The Sensitivity of Supercell Cold Pools to the Lifting Condensation Level and the Predicted Particle Properties Microphysics Scheme

SHAWN S. MURDZEK,[a] YVETTE P. RICHARDSON,[a] AND PAUL M. MARKOWSKI[a]

[a] *Department of Meteorology and Atmospheric Science, The Pennsylvania State University, University Park, Pennsylvania*

(Manuscript received 28 April 2023, in final form 22 December 2023, accepted 21 February 2024)

ABSTRACT: Previous work found that cold pools in ordinary convection are more sensitive to the microphysics scheme when the lifting condensation level (LCL) is higher owing to a greater evaporation potential, which magnifies microphysical uncertainties. In the current study, we explore whether the same reasoning can be applied to supercellular cold pools. To do this, four perturbed-microphysics ensembles are run, with each using an environment with a different LCL. Similar to ordinary convection, the sensitivity of supercellular cold pools to the microphysics increases with higher LCLs, though the physical reasoning for this increase in sensitivity differs from a previous study. Using buoyancy budgets along parcel trajectories that terminate in the cold pool, we find that negative buoyancy generated by microphysical cooling is partially countered by a decrease in environmental potential temperatures as the parcel descends. This partial erosion of negative buoyancy as parcels descend is most pronounced in the low-LCL storms, which have steeper vertical profiles of environmental potential temperature in the lower atmosphere. When this erosion is accounted for, the strength of the strongest cold pools in the low-LCL ensemble is reduced, resulting in a narrower distribution of cold pool strengths. This narrower distribution is indicative of reduced sensitivity to the microphysics. These results suggest that supercell behavior and supercell hazards (e.g., tornadoes) may be more predictable in low-LCL environments.

SIGNIFICANCE STATEMENT: Thunderstorms typically produce "pools" of cold air beneath them owing in part to the evaporation of rain and melting of ice produced by the storm. Past work has found that in computer simulations of thunderstorms, the cold pools that form beneath thunderstorms are sensitive to how rain and ice are modeled in the simulation. In this study, we show that in the strongest thunderstorms that are capable of producing tornadoes, this sensitivity is reduced when the humidity in the lowest few kilometers above the surface is increased. Exploring why the sensitivity is reduced when the humidity increases provides a deeper understanding of the relationship between humidity and cold pool strength, which is important for severe storm forecasting.

KEYWORDS: Cold pools; Supercells; Cloud microphysics; Cloud-resolving models

1. Introduction

Cloud microphysics, which are processes that involve individual hydrometeors, play an important role in the physics of supercell thunderstorms. Microphysical processes directly impact storm thermodynamics through the enthalpies associated with the phase changes of water, and this modification of the thermodynamics affects storm dynamics. In addition to influencing the thermodynamics and dynamics of a storm, microphysical processes also play an important role in many of the hazards associated with supercells, such as tornadoes (e.g., Snook and Xue 2008; Dawson et al. 2016), hail, and lightning.

Microphysical processes must be parameterized in numerical simulations of supercells because the grid spacings of these simulations (tens of meters up to a few kilometers, e.g., Orf et al. 2017; Dowell et al. 2022) prevent both microphysical processes and other atmospheric processes that influence clouds (e.g., turbulence) from being fully resolved (Morrison et al. 2020). Many different microphysics schemes (i.e., a collection of parameterizations for various microphysical processes) exist, and each handles various processes and hydrometeor properties differently (e.g., Morrison et al. 2009; Mansell et al. 2010; Morrison and Milbrandt 2015). Some of these decisions about how to configure a microphysics scheme arise from trade-offs between computational efficiency and physical realism. For example, bulk-type microphysics schemes tend to be more realistic when more moments of the particle size distribution (PSD) are predicted (Dawson et al. 2010), but predicting more moments comes with more computational overhead. Other scheme configuration decisions arise from having to parameterize processes that are not easily parameterized or understood, such as raindrop breakup (Milbrandt and Yau 2005; Morrison et al. 2012; Saleeby et al. 2022). Unfortunately, several studies have demonstrated that supercell simulations are sensitive to how a microphysics scheme is configured (e.g., Johnson et al. 1993; Gilmore et al. 2004b; van den Heever and Cotton 2004; Snook and Xue 2008; Dawson et al. 2010; Morrison and Milbrandt 2011; Van Weverberg 2013; Freeman et al. 2019; Kacan and Lebo 2019; Mansell et al. 2020; Milbrandt et al. 2021), and it is not clear which of these configurations is the most "correct."

Murdzek's current affiliation: Cooperative Institute for Research in Environmental Sciences, University of Colorado Boulder and NOAA/Global Systems Laboratory, Boulder, Colorado.

Corresponding author: Shawn S. Murdzek, shawn.s.murdzek@noaa.gov

DOI: 10.1175/MWR-D-23-0092.1

This uncertainty in microphysics schemes results in forecast uncertainty for supercells and their associated hazards.

The inspiration behind this study is not to document additional sensitivities of supercell simulations to the microphysics scheme. Instead, our goal is to identify environments where supercells are less sensitive to microphysical processes, which indicates increased predictability. Prior work has demonstrated that the sensitivity of convective storms to the microphysics changes with the environmental wind shear (Gilmore et al. 2004a,b; Morrison et al. 2012), precipitable water (Cohen and McCaul 2006), convective available potential energy (CAPE; Van Weverberg 2013; Morrison et al. 2015), and lifting condensation level (LCL; Murdzek et al. 2022, hereinafter M22). The present study examines whether the sensitivity of simulated supercell cold pools to the microphysics changes with the environmental LCL. This is an extension of M22, who found that the sensitivity of cold pools in ordinary convection to the microphysics increases with higher LCLs. The physical reasoning was that higher LCLs are associated with a drier planetary boundary layer (PBL), which results in more rain evaporation compared to low-LCL environments. This greater evaporation potential exaggerated the microphysical uncertainty, resulting in a greater sensitivity to the microphysics. This study will examine whether this same reasoning can be applied to supercells.

As with M22, the focus here is on cold pools. The reason for this is twofold. First, cold pools are directly linked to the microphysics through the enthalpies associated with the phase changes of water (James and Markowski 2010; Mallinson and Lasher-Trapp 2019), which makes cold pool strength a convenient diagnostic to measure the sensitivity of supercells to the microphysics. Second, cold pools play a vital role in tornadogenesis, with the probability of tornadogenesis generally decreasing as the cold pool becomes more negatively buoyant, which impedes the stretching of near-surface, circulation-rich air to tornado strength (e.g., Markowski et al. 2002; Shabbott and Markowski 2006; Grzych et al. 2007; Markowski and Richardson 2014). It is possible that supercells that are less sensitive to the microphysics are also less volatile when it comes to tornado production (e.g., Coffer et al. 2017). If this is true, then environments where supercells are less sensitive to the microphysics may be tornado forecasts of opportunity.

In addition to extending M22 to supercells, we also seek to better understand the connection between the LCL and cold pool strength. Observations have shown that cold pool strength tends to increase with larger inflow surface dewpoint depressions (Markowski et al. 2002; Shabbott and Markowski 2006; McDonald and Weiss 2021), which are associated with higher LCLs. This relationship between cold pool strength and LCL has also been shown in several modeling studies, with the explanation that higher LCLs are associated with more rain evaporational cooling (McCaul and Cohen 2002; Markowski et al. 2003; Brown and Nowotarski 2019; M22). Generally, the amount of rain evaporation in a given volume of air depends on two factors: the environmental humidity of that volume (the "environmental control" on evaporation) and the characteristics of the rain PSDs (the "microphysical control" on evaporation). The LCL is related to both of these factors. In regard to the environmental control, higher LCLs are generally associated with lower relative humidity, which, all else being equal, increases rain evaporation. This is the physical argument that is typically used to help explain why high-LCL environments are less favorable for tornadogenesis: higher LCLs result in more evaporational cooling, which contributes to cold pools with excessive negative buoyancy that impedes vertical vorticity stretching (e.g., Markowski et al. 2003). In regard to the microphysical control, the LCL can impact upstream microphysical processes which, in turn, influence the rain PSD. For example, a lower LCL might result in a deeper warm-cloud depth,[1] which would allow for more warm-rain processes to occur. This would then influence the downstream rain PSDs and, therefore, rain evaporation. In M22, storms in low-LCL environments produced slightly more rain evaporation when only accounting for the microphysical control, though this trend was overwhelmed by the environmental control, which favored more evaporation in high-LCL environments. In Lerach and Cotton (2012), precipitation rates decreased—resulting in weaker cold pools—with higher LCLs, which is an example of the microphysical control exceeding the environmental control. Thus, a higher LCL does not always guarantee a colder cold pool.

It is clear that the LCL influences rain evaporation, but how much of this cooling from evaporation contributes to near-surface cold pool strength? Mallinson and Lasher-Trapp (2019) showed that graupel sublimation was the dominant factor contributing to cooling within downdrafts, but rain evaporation was better correlated with near-surface cold pool strength. Graupel sublimation tends to occur at higher altitudes than rain evaporation, which suggests that microphysical cooling aloft may have a reduced impact on near-surface cold pool strength compared to cooling at lower altitudes. Analogously, evaporational cooling that occurs near cloud base may have a reduced impact on cold pool strength compared to evaporational cooling that occurs at lower levels. Thus, more rain evaporation might not always result in a stronger near-surface cold pool, which adds a layer of complexity to the explanation that high-LCL storms produce stronger cold pools owing to more rain evaporation. This suggests that we need a deeper understanding of the processes that influence cold pool development in supercells and how the relative strength of these processes changes with LCL.

Based on the preceding discussion, our research questions are as follows:

1) What are the primary drivers of supercell cold pool strength?
2) How does the magnitude of these drivers change as the LCL varies?
3) Does the sensitivity of supercell cold pools to the microphysics increase as the LCL increases? Is the physical reasoning similar to M22?

After detailing the methods in the next section, we will perform several Eulerian analyses. Owing to several shortcomings of the Eulerian analyses, a Lagrangian analysis will then be performed

[1] Distance between cloud base and the freezing level.

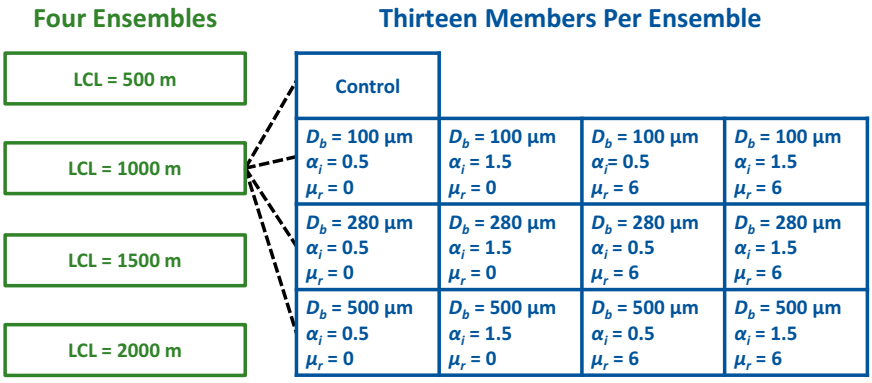

FIG. 1. Schematic detailing the various simulations. The green boxes on the left indicate the different ensembles, while the blue boxes on the right indicate the members within a sample ensemble. The raindrop breakup threshold D_b, ice fall speed multiplier α_i, and rain PSD shape parameter μ_r for each ensemble member are listed in the blue boxes on the right.

to better answer our research questions. The results are summarized in the final section.

2. Methods

Following the approach of M22, perturbed-microphysics ensembles with varying LCLs are created to capture how the sensitivity to the microphysics varies with the LCL. A total of four ensembles with LCLs between 500 and 2000 m are analyzed, with each ensemble consisting of 13 members that each use a different configuration of the predicted particle properties (P3; Morrison and Milbrandt 2015; Milbrandt and Morrison 2016) microphysics scheme (Fig. 1). Within this framework, the ensemble spread is used as a proxy for the sensitivity to the microphysics. Comparing the ensemble spread between ensembles indicates how the sensitivity to the microphysics changes with the LCL. Each ensemble member is a Cloud Model 1, release 20.1 (CM1; Bryan and Fritsch 2002; Bryan 2021), simulation, with the model configuration listed in Table 1.

Each ensemble member is initialized using a horizontally homogeneous base state. All simulations use the same base-state wind profile, which consists of a shear vector that undergoes a quarter turn between 0 and 2 km AGL and unidirectional, westerly shear between 2 and 6 km AGL (Fig. 2). This wind profile is favorable for supercells (Table 2), but only marginally favorable for tornadoes, with a 0–500-m storm-relative helicity of only 77.9 $m^2 s^{-2}$ (cf. Fig. 2 from Coffer et al. 2019). Each ensemble uses a different base-state thermodynamic profile with a different LCL while holding the level of free convection (LFC) and pseudoadiabatic CAPE approximately constant (Table 3). These base states are constructed using the methodology of McCaul and Cohen (2002), which results in three layers: 1) the PBL, which consists of a well-mixed layer beneath a nearly moist-adiabatic layer, 2) the free troposphere, which follows the prescribed buoyancy profile of McCaul and Weisman (2001), and 3) an isothermal stratosphere. The parameters used to create the thermodynamic profiles and various sounding metrics are listed in Table 3. The resulting thermodynamic base states (Fig. 2) are very similar to those used in Murdzek et al. (2021) and M22, except that the static stability is increased in the lower troposphere to prevent Kelvin–Helmholtz instability, which could result in excessive mixing and cause the environment experienced by the storm to differ from the prescribed environment.

Each simulation uses a moving domain in order to keep the supercell near the origin of the grid. All members within a given ensemble use the same domain motion, which is the average storm motion of the control member. The average storm motion for each control member is determined by tracking the midlevel mesocyclone of the dominant right-moving supercell using an objective mesocyclone detection algorithm. This algorithm defines the mesocyclone center as the 2–5-km updraft helicity (UH)-weighted centroid of the largest, continuous area with UH > 50 $m^2 s^{-2}$, which is similar to the approach used in Peters et al. (2019). The midlevel mesocyclone location is constrained in time such that the location must be within 3 km of the mesocyclone location determined 30 s earlier.

TABLE 1. CM1 configuration.

Parameter	Value
Domain size	120 km × 120 km × 18 km
Horizontal grid spacing	200 m
Vertical grid spacing	50 m below 2.5 km 500 m above 13.5 km
Integration length	2 h
Initial large time step	2.0 s
Adaptive time step?	Yes
Lateral boundary conditions	Open-radiative
Top and bottom boundary conditions	Free slip
Initiation method	Updraft nudging with $w_{max} = 10$ m s^{-1}
Microphysics	Predicted particle properties
Radiation	None
Surface fluxes	None
Coriolis acceleration	None
3D output frequency	300 s
Stats output frequency	30 s

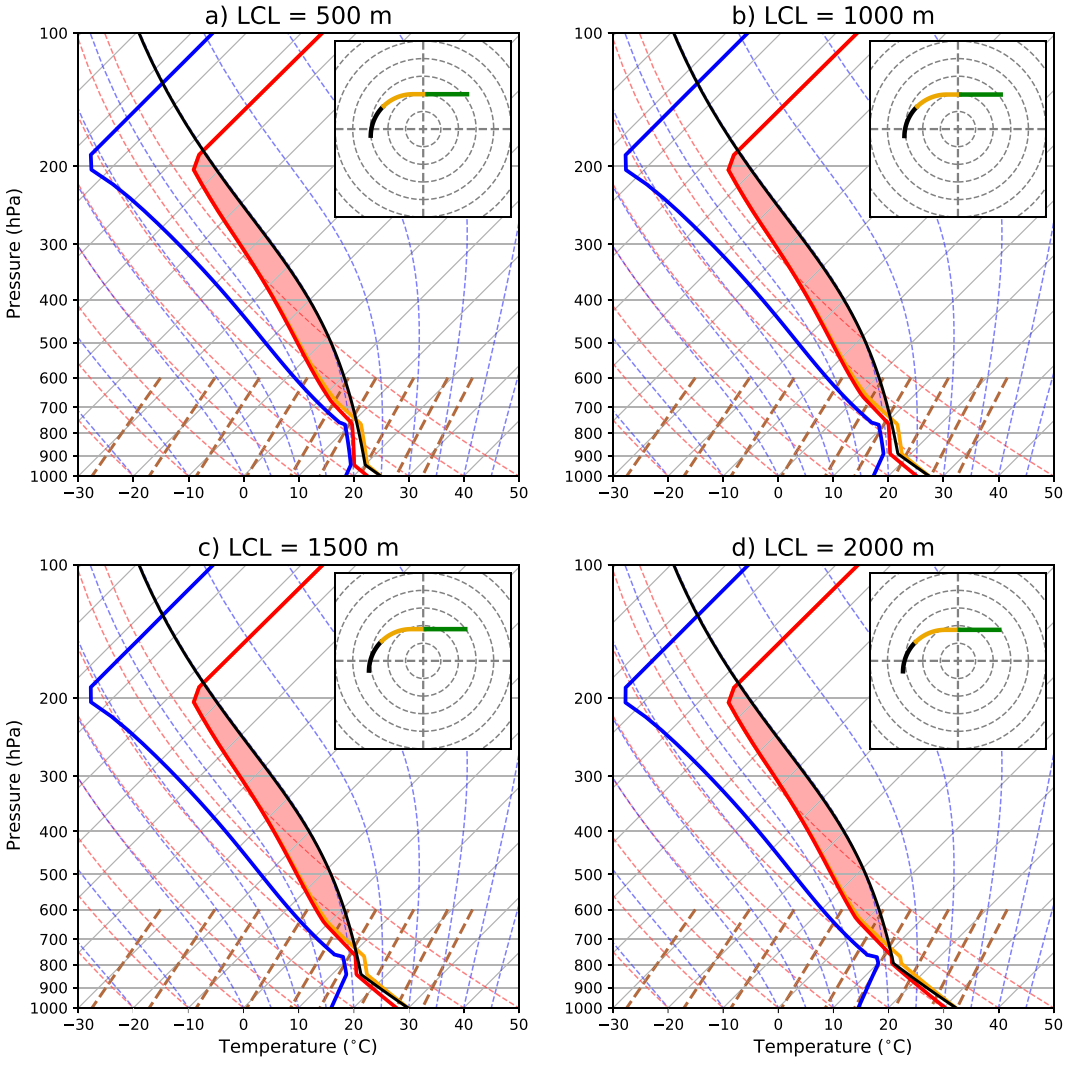

FIG. 2. Base-state environments for the LCL = (a) 500, (b) 1000, (c) 1500, and (d) 2000 m ensembles. The solid red, blue, orange, and black lines on the skew T–log$p$ diagram represent the environmental temperature, environmental dewpoint, environmental virtual temperature, and virtual temperature profile for a surface-based parcel, respectively. The shaded red area is proportional to the CAPE. The hodograph is storm relative with the origin as the approximate storm motion. Each dashed ring is 5 m s^{-1}, and the black, gold, and green lines denote the storm-relative winds between 0–1, 1–3, and 3–6 km AGL, respectively.

The midlevel mesocyclone location is also used to determine cold pool strength. Our focus is on the near-surface cold pool, so we define the cold pool as the area at the lowest model level (LML; 25 m AGL) with a perturbation potential temperature $\theta' < -1$ K. To eliminate cold pools from spurious convection that might be occurring elsewhere in the domain, the cold pool is restricted to be within 30 km of the midlevel mesocyclone. Cold pool strength is then defined as the sum of all buoyancy B values within the cold pool and is denoted $\Sigma B_{\text{sfc,CP}}$. Other measures of cold pool strength (e.g., minimum θ', average θ' in the cold pool, and sum of all B values within the cold pool up to a height of 2 km AGL) and other distances from the midlevel mesocyclone (4 and 10 km) were also tested, and using these other metrics does not change the qualitative results presented here (Fig. 4.9 from Murdzek 2022).

The last piece of the ensemble setup is the perturbations applied to the P3 microphysics scheme. The P3 scheme used

TABLE 2. Base-state bulk wind differences (BWD) and storm-relative helicities (SRHs) computed over various depths.

0–6-km BWD (m s^{-1})	0–1-km BWD (m s^{-1})	0–0.5-km SRH (m^2 s^{-2})	0–1-km SRH (m^2 s^{-2})	0–3-km SRH (m^2 s^{-2})
30.5	9.2	77.9	146.1	282.4

TABLE 3. Thermodynamic base-state parameters and parameters used to create the base-state thermodynamic profiles. LCL, LFC, equilibrium level (EL), CAPE, and CIN are computed for a surface-based parcel following pseudoadiabatic ascent (computations include the virtual temperature correction). Other parameters include the surface pressure p_{sfc}, surface temperature T_{sfc}, absolute supersaturation at the LML ($s_0 = q_v - q_{sl}$, where q_v is the water vapor mass mixing ratio and q_{sl} is the equilibrium water vapor mass mixing ratio), and the PBL lapse rate (PBL LR).

LCL (m)	LFC (m)	EL (m)	CAPE (J kg^{-1})	CIN (J kg^{-1})	p_{sfc} (hPa)	T_{sfc} (K)	PBL LR (K km^{-1})	s_0 (g kg^{-1})
500	2491	12 402	1971	37.8	1000	295.66	8.9	−3.63
1000	2568	12 405	1971	54.3	1000	298.3	8.9	−7.78
1500	2642	12 408	1971	66.6	1000	300.92	8.9	−12.36
2000	2707	12 411	1971	74.0	1000	303.49	8.9	−17.38

herein for the control member of each ensemble is identical to the CM1r20.1 configuration with three exceptions: 1) shedding of raindrops from ice collecting rain at temperatures above 273.15 K is turned on, 2) wet growth is moved up within the P3 code, so wet growth can be used to alter the ice–ice collection efficiency, and 3) the maximum allowed mean raindrop size $D_{m,r}$ is increased from 0.8 to 4 mm following the recommendations of Johnson et al. (2019). After applying these changes, a series of tests are performed to determine the sensitivity of supercell cold pools to various parameters within P3. Out of the 12 parameters screened (see the appendix), cold pools are found to be most sensitive to the raindrop breakup threshold D_b, the ice fall speed multiplier α_i,[2] and the rain PSD shape parameter μ_r. A total of three D_b values, two α_i values, and two μ_r values are selected, resulting in 12 different P3 realizations. Adding the control simulation ($D_b = 280$ μm, $\alpha_i = 1$, and $\mu_r = 0$) results in 13 total members for each ensemble (Fig. 1).

Trajectories and buoyancy budgets

Past studies (e.g., Klemp et al. 1981; Dawson et al. 2016; Torri and Kuang 2016; Betten et al. 2017) have found great utility in using parcel trajectories to better understand the nature of intrastorm airflows. We follow a similar approach here by using buoyancy budgets along parcel trajectories to probe the origins of supercell cold pools. To perform the parcel analysis, all members from the LCL = 500 m and LCL = 2000 m ensembles as well as the control members of the LCL = 1000 m and LCL = 1500 m ensembles are restarted at 5400 s, with 1 141 560 parcels seeded within a box with the dimensions $x \in [-15, 15]$ km, $y \in [-10, 15]$ km, and $z \in [0.1, 6]$ km. These parcels have an initial spacing of 0.2, 0.2, and 0.1 km in the x, y, and z directions, respectively, and are integrated forward in time using the model time step for 1800 s with trajectory output being saved every 15 s. Cold pool parcels are then identified at analysis times that start at 5400 s and continue for 1800 s with a 30-s cadence. The criteria for cold pool parcels are as follows:

1) Parcel B at 5400 s is > -0.01 m s^{-2}.
2) Parcel θ' at the analysis time is < -1 K.
3) Parcel is within 30 km of the midlevel mesocyclone at the analysis time.
4) Parcel height at the analysis time is between 25 and 50 m AGL.
5) Parcel never dipped below the LML between 5400 s and the analysis time.
6) Parcel has not already been selected as a cold pool parcel.

Criteria 2–4 ensure that the parcel terminates within the cold pool, while criterion 6 prevents double-counting and criterion 5 eliminates parcels that might have errors in the trajectory calculation owing to extrapolation. Criterion 1 is included because we are interested in the development of large, negative B along parcel trajectories and parcels that already have large negative B at the initial time preclude such an investigation.

We are ultimately interested in learning how these parcels became negatively buoyant. To do this, we derive a B budget equation, which starts with the B equation in CM1 (Bryan 2021):

$$B = g\left[\frac{\theta'}{\theta_0} + \left(\frac{1}{\epsilon} - 1\right)(q_v - q_{v0}) - q_{tot}\right], \tag{1}$$

where g is the gravitational acceleration, ϵ is the ratio of the dry-air and water-vapor gas constants, q_v is the water-vapor mass mixing ratio, q_{tot} is the hydrometeor mass mixing ratio, and variables with the subscript 0 denote the base-state values, which are functions of z. The total derivative of Eq. (1) is taken with respect to time, which results in

$$\frac{dB}{dt} = g\left[\frac{1}{\theta_0^2}\left(\theta_0\frac{d\theta}{dt} - \theta\frac{d\theta_0}{dt}\right) + \left(\frac{1}{\epsilon} - 1\right)\left(\frac{dq_v}{dt} - \frac{dq_{v0}}{dt}\right) - \frac{dq_{tot}}{dt}\right]. \tag{2}$$

From here, Eq. (2) is integrated over a parcel trajectory to compute the final B at time t_f, $B(t_f)$, assuming an initial B of $B(t_i)$ at time t_i. The final result is

$$B(t_f) = B(t_i) + \underbrace{g\int_{t_i}^{t_f}\frac{1}{\theta_0}\frac{d\theta}{dt}dt}_{\theta\text{ term}} - \underbrace{g\int_{t_i}^{t_f}\frac{\theta}{\theta_0^2}\frac{d\theta_0}{dt}dt}_{\theta_0\text{ term}} + \underbrace{g\left(\frac{1}{\epsilon} - 1\right)\Delta q_v}_{q_v\text{ term}} - \underbrace{g\left(\frac{1}{\epsilon} - 1\right)\Delta q_{v0}}_{q_{v0}\text{ term}} - \underbrace{g\Delta q_{tot}}_{q_{tot}\text{ term}}, \tag{3}$$

where Δ denotes the difference between the final and initial values along a parcel trajectory. In Eq. (3), the five terms on

[2] The ice fall speed multiplier was added to P3 to account for ice fall speed uncertainty. The values tested were 0.5, 1, and 1.5, which is within the range used by Stanford et al. (2019).

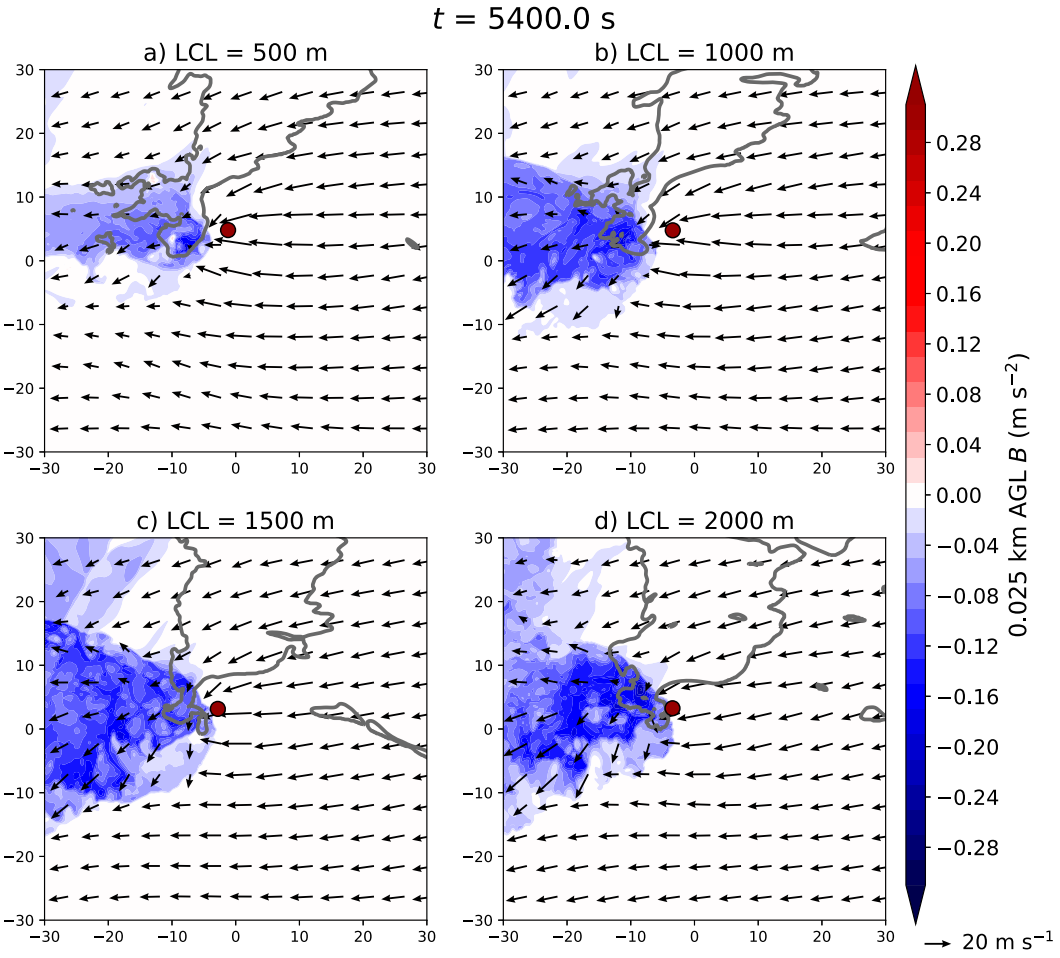

FIG. 3. Horizontal cross sections from the control member of each ensemble at 5400 s. Color shading represents LML buoyancy, vectors represent LML horizontal winds, the gray contour represents the 25-dBZ reflectivity contour at 1 km AGL, and the maroon dot indicates the objectively analyzed mesocyclone center. Axis labels are in kilometers.

the right-hand side after $B(t_i)$ will be referred to as the θ term, θ_0 term, q_v term, q_{v0} term, and q_{tot} term, respectively.

The B budgets are computed offline using the 15-s parcel output. Time derivatives are computed using second-order finite differences while the time integrals are computed using a trapezoidal method. As shown in section 4, the residuals of these budgets are two orders of magnitude less than the final B values, which gives us confidence in the budgets. In addition to B budgets, the θ and q_v budget terms, which are already computed within CM1, are also interpolated to the parcel trajectories and integrated in time using a trapezoidal method to obtain θ and q_v budgets.

3. Eulerian analysis

Each simulation produces convection resembling a supercell that lasts for at least 2 h. Horizontal cross sections of the control members from each ensemble show features typical of supercells, including a rear-flank gust front [near (−5, −5) in each of the panels in Fig. 3] and a "hook" echo (immediately west of the maroon dots in Fig. 3). Furthermore, the objective midlevel mesocyclone detection algorithm produces realistic mesocyclone locations (maroon dots in Fig. 3), which gives us confidence that the algorithm is performing properly. For all simulations, a midlevel mesocyclone is detected soon after model initialization and lasts until the end of the 2-h integration window.

Time series of ensemble medians and standard deviations of cold pool strength are used to assess how the LCL impacts cold pool strength and sensitivity to the microphysics scheme. As documented in the previous literature (e.g., McCaul and Cohen 2002; Brown and Nowotarski 2019), cold pool strength tends to increase as the LCL increases (Fig. 4a), though this trend is somewhat muddied by the LCL = 2000 m ensemble, which has a weaker median cold pool strength than the LCL = 1500 m ensemble. As was found in the ordinary convection simulations of M22, the ensemble spread of cold pool strength also tends to increase as the LCL increases (Fig. 4b). In fact, the ratio of the LCL = 2000 m standard deviation to the LCL = 500 m standard deviation is greater than one and

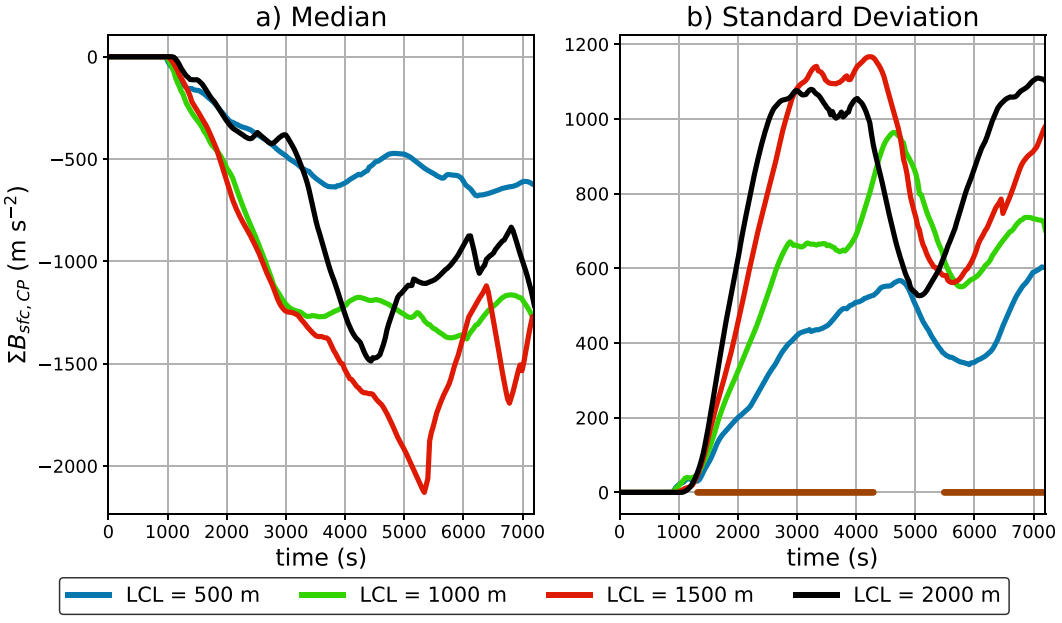

FIG. 4. Time series of ensemble cold pool statistics. (a) Ensemble medians and (b) ensemble standard deviations of $\Sigma B_{\text{sfc,CP}}$. The brown line along the x axis in (b) denotes times when the ratio of the standard deviation of the LCL = 2000 m ensemble to the LCL = 500 m ensemble is greater than one and statistically significant at the 95% confidence level. The cold pool is defined as all grid points at the LML within 30 km of the midlevel mesocyclone with $\theta' < -1$ K.

statistically significant at the 95% confidence level using a bootstrap resampling test (Wilks 2011, chapter 5.3.5) for the majority of the time after cold pool onset. Altogether, these results suggest that the sensitivity of supercell simulations to the microphysics increases with higher LCLs, which agrees with M22.

Vertical profiles of microphysical processes

We now turn to *why* cold pool strength and sensitivity of the cold pool to the microphysics increase with higher LCLs. The first tool that will be used is vertical profiles of microphysical processes. Vertical profiles of ensemble-median cooling from cloud evaporation Q_{evac}, rain evaporation Q_{evar}, melting Q_{melt}, and sublimation Q_{subl} show that Q_{evar} is the dominant cooling mechanism beneath cloud base (Figs. 5a,c,e,g). This suggests that Q_{evar} might be the main process driving cold pool strength, but we cannot be certain because parcels contributing to the cold pool might have experienced considerable cooling aloft from melting and sublimation before sinking to the surface, which is not captured in this Eulerian analysis. The Lagrangian analyses provided later in section 4 will address this shortcoming. When comparing across the four ensembles, Q_{evar} tends to increase slightly as the LCL increases from 500 to 1500 m, which agrees with the hypothesis that high-LCL storms tend to produce stronger cold pools owing to more evaporational cooling (McCaul and Cohen 2002; M22), though this trend is less pronounced compared to M22. This trend is also upended by the LCL = 2000 m ensemble, which features a median Q_{evar} that is similar to the LCL = 500 m ensemble, at least below 1 km AGL (Fig. 5c). This is a bit surprising given that the LCL = 2000 m ensemble tends to have a stronger cold pool than the LCL = 500 m ensemble (Fig. 4a). These observations suggest that Q_{evar} is not the only factor contributing to cold pool strength.

Shifting the focus to the increase in the ensemble spread of cold pool strength with higher LCLs, we find that the ensemble standard deviation of rain evaporation does not clearly increase with LCL (Fig. 5d). This deviates from M22, in which the ensemble spread of rain evaporation increases with LCL (see their Fig. 14d). M22 argued that higher LCLs result in a greater evaporation potential owing to the drier conditions in the PBL, which exaggerate any microphysical differences within an ensemble, resulting in a larger spread of rain evaporation rates. Based on Fig. 5d, this mechanism does not appear to be occurring here.

To help explain why ensemble medians and standard deviations of Q_{evar} in our simulations do not increase strongly with LCL, we explore the different factors in the rain evaporation equation. The equation for rain evaporation in P3 when $T > 273.15$ K is [see Eqs. (C6) and (C4) in Morrison and Milbrandt (2015)]:

$$\frac{\partial q_r}{\partial t} = A_c \frac{\tau}{\tau_r \Gamma_l} + (\delta_0 - A_c \tau) \frac{\tau}{\Delta t \tau_r \Gamma_l} (1 - e^{-\Delta t/\tau}), \tag{4}$$

where q_r is the rain mass mixing ratio.

$$A_c = \frac{\partial q_v}{\partial t} + \frac{dq_{\text{sl}}}{dT} \frac{dT}{dt}. \tag{5}$$

τ is the multiphase supersaturation relaxation time, τ_r is the phase relaxation time for rain, Γ_l is the psychrometric correction, δ_0 is the supersaturation passed to the microphysics scheme by CM1, Δt is the model time step, and q_{sl} is the equilibrium water vapor mass mixing ratio with respect to

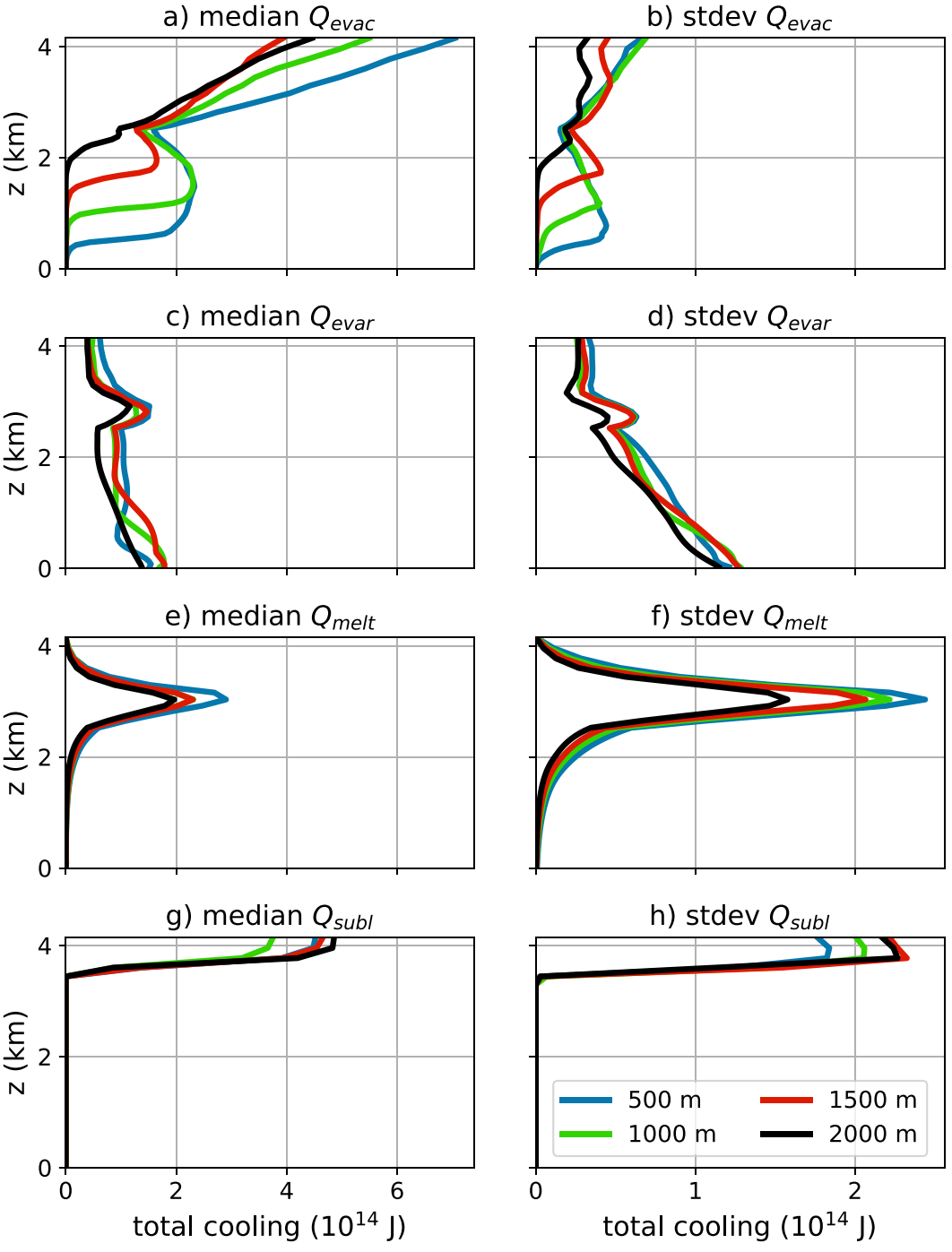

FIG. 5. Vertical profiles of total cooling from various microphysical processes. (a),(c),(e),(g) Ensemble medians and (b),(d),(f),(h) ensemble standard deviations. Microphysical processes include (a),(b) cloud evaporation, (c),(d) rain evaporation, (e),(f) melting, and (g),(h) sublimation. Profiles are computed during the entire 2-h integration period for all grid points within 30 km of the midlevel mesocyclone.

liquid water. Similar to M22, we seek to isolate the microphysical and environmental controls on evaporation. The microphysical control is related to the shapes of the hydrometeor PSDs and is tied to τ and τ_r. The environmental control, on the other hand, is related to the humidity and is tied to δ_0. For completeness, we will also examine the impact of A_c on evaporation. Rain evaporation is computed offline for each simulation while holding either τ and τ_r constant, A_c constant, or δ_0 constant. The resulting profiles of Q_{evar} are shown in Fig. 6, along with vertical profiles of Q_{evar} when no factors are held

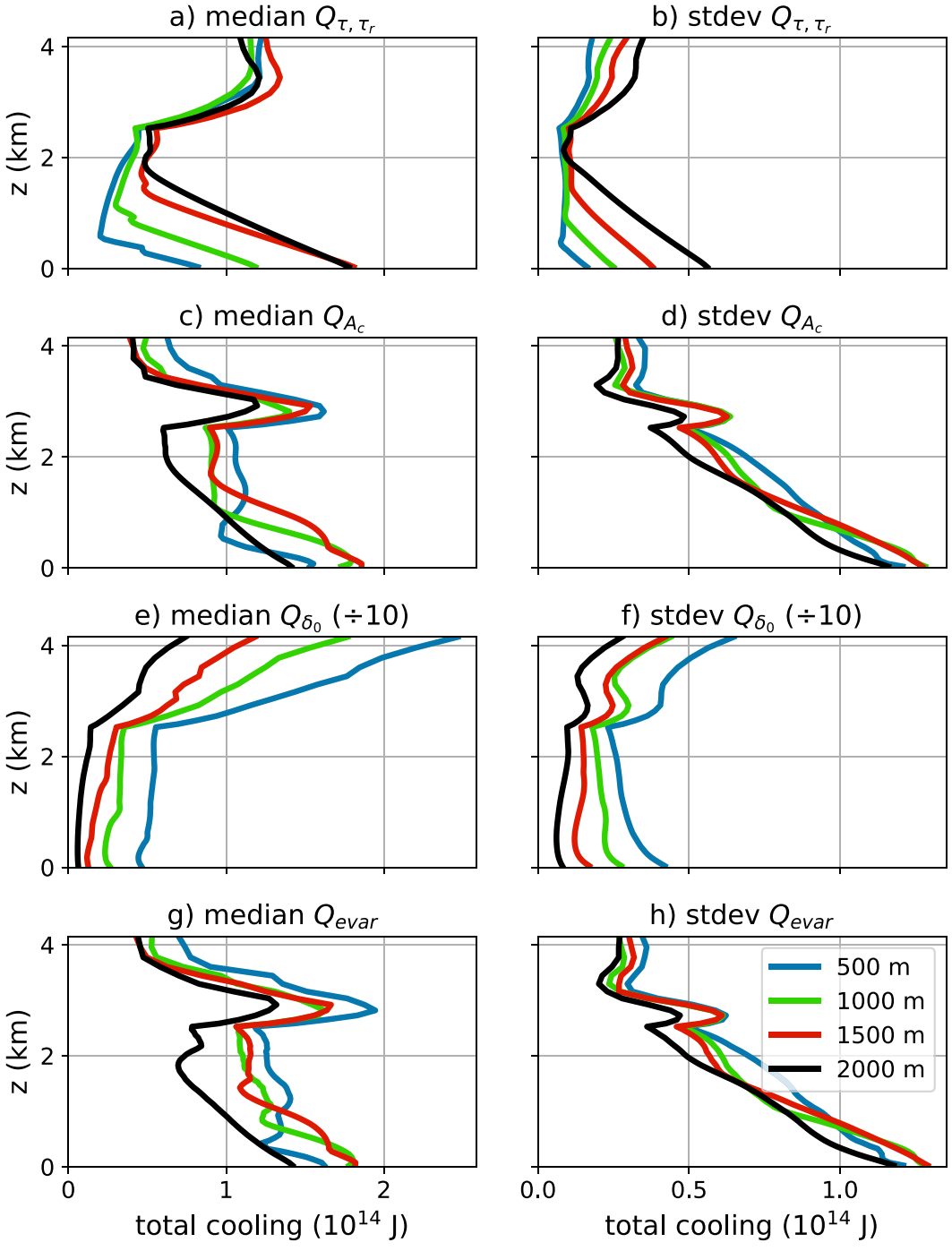

FIG. 6. As in Fig. 5, but with rain evaporation computed while holding (a),(b) τ and τ_r constant, (c),(d) A_c constant, and (e),(f) δ_0 constant and (g),(h) without holding any of the factors constant.

constant, which are included to show the accuracy of these offline computations (cf. Figs. 5c,d). When the microphysical control is held constant, both the ensemble median and standard deviation increase with higher LCLs, likely owing to the drier conditions in the high-LCL simulations (Figs. 6a,b). When the environmental control is held constant, the opposite is true (Figs. 6e,f), which suggests that the rain PSDs are more favorable for evaporation in the low-LCL simulations. Holding A_c constant has little impact on the rain evaporation trends (Figs. 6c,d). These results agree with M22, who found that the environmental control favors greater evaporation in high-LCL simulations and the microphysical control

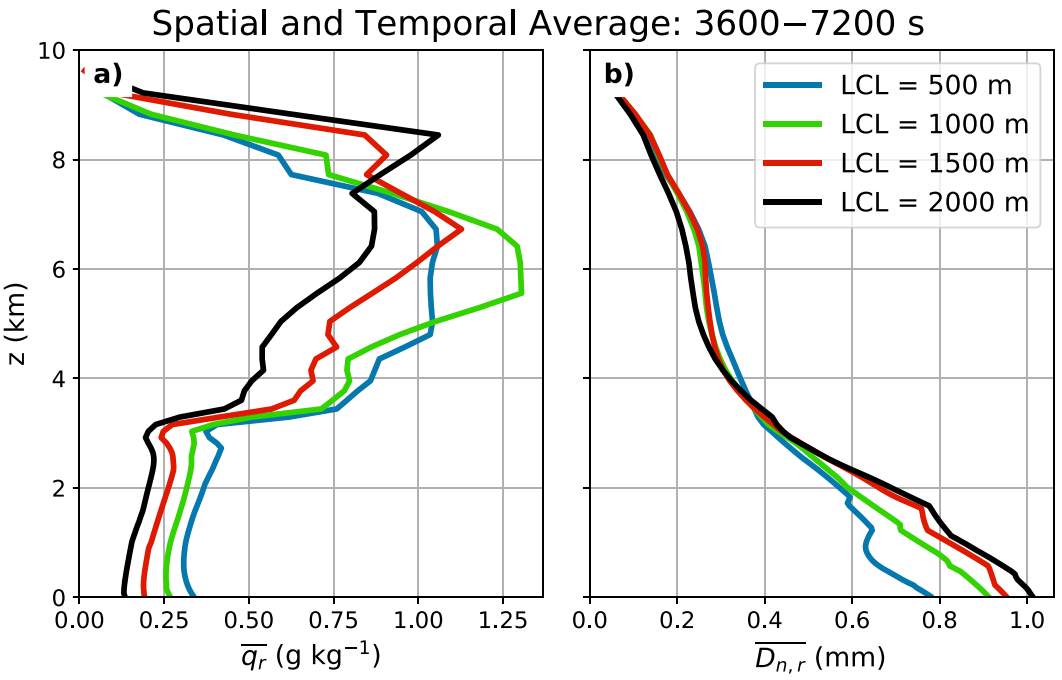

FIG. 7. Ensemble medians of various rain PSD characteristics. (a) Horizontally and temporally averaged rainwater mass mixing ratios $\overline{q_r}$ and (b) horizontally and temporally averaged number-weighted mean raindrop diameters $\overline{D_{n,r}}$. Averages are performed during the second hour of the simulations using only those grid points with $q_r > 0.01$ g kg^{-1}.

favors greater evaporation in low-LCL simulations. Unlike M22, however, the environmental control does not dominate the microphysical control, which helps explain why the ensemble median and standard deviation of Q_{evar} do not clearly increase with higher LCLs. Put another way, in the supercell simulations, the additional evaporation expected from increasing the LCL owing to a decrease in relative humidity is balanced by rain PSD characteristics that become increasingly less favorable for evaporation as the LCL is raised.

To understand why the microphysical control varies more with LCL in these supercell simulations compared to the ordinary convection simulations of M22, we will examine bulk rain PSD characteristics from each of the ensembles. As the LCL decreases, two aspects of the rain PSDs favor more rain evaporational cooling. The first is an increase in the average q_r as the LCL decreases (Fig. 7a), which results in more rain mass that can be evaporated. The second is a decrease in the average number-weighted mean raindrop diameter $D_{n,r}$ as the LCL decreases (Fig. 7b). This decrease in $D_{n,r}$ coupled with the increase in q_r with lower LCLs is indicative of more numerous and smaller drops with a larger surface area-to-volume ratio, which favors more evaporation (e.g., van den Heever and Cotton 2004; Snook and Xue 2008). This decrease in how favorable the rain PSDs are for rain evaporation with higher LCLs is likely also the reason why the LCL = 2000 m ensemble did not have the strongest cold pool out of the four ensembles. In the ordinary convection simulations, on the other hand, total rainfall and $D_{n,r}$ do not vary much with LCL (e.g., Fig. 18 from M22), which results in less variability in the microphysical control in those simulations.

A number of factors are likely contributing to the differences in rain characteristics between the different ensembles. One factor is that precipitable water tends to decrease with higher LCLs in our base-state environments (not shown), which would contribute to a decrease in rain as the LCL increases. Additional factors can be gleaned from rain mass budgets from each of the control simulations (Fig. 8). One of the most striking differences between the simulations is that as the LCL increases, the percentage of rain mass lost to freezing increases while the percentage of rain gained from melting stays relatively constant (Figs. 8c,f). The larger percentages of rain mass lost to freezing in the high-LCL simulations are possibly tied to the shallower warm-cloud depth,[3] which might prevent liquid drops from growing large enough to fall out before being advected above the freezing level. The reason behind the lack of a compensating increase in rain gained from melting with higher LCLs is not clear from these budgets and is beyond the scope of the current study, though it is possible that the newly nucleated ice particles in the high-LCL simulations are smaller than those in the low-LCL simulations owing to the shallower warm-cloud depths in the high-LCL simulations. These smaller ice particles could then be lofted higher in the supercell where they are more likely to be advected horizontally and sublimate rather than falling back down to the melting layer. The impact of freezing and

[3] Warm-cloud depth decreases as the LCL increases in our base states because the freezing level is approximately the same in all the base states.

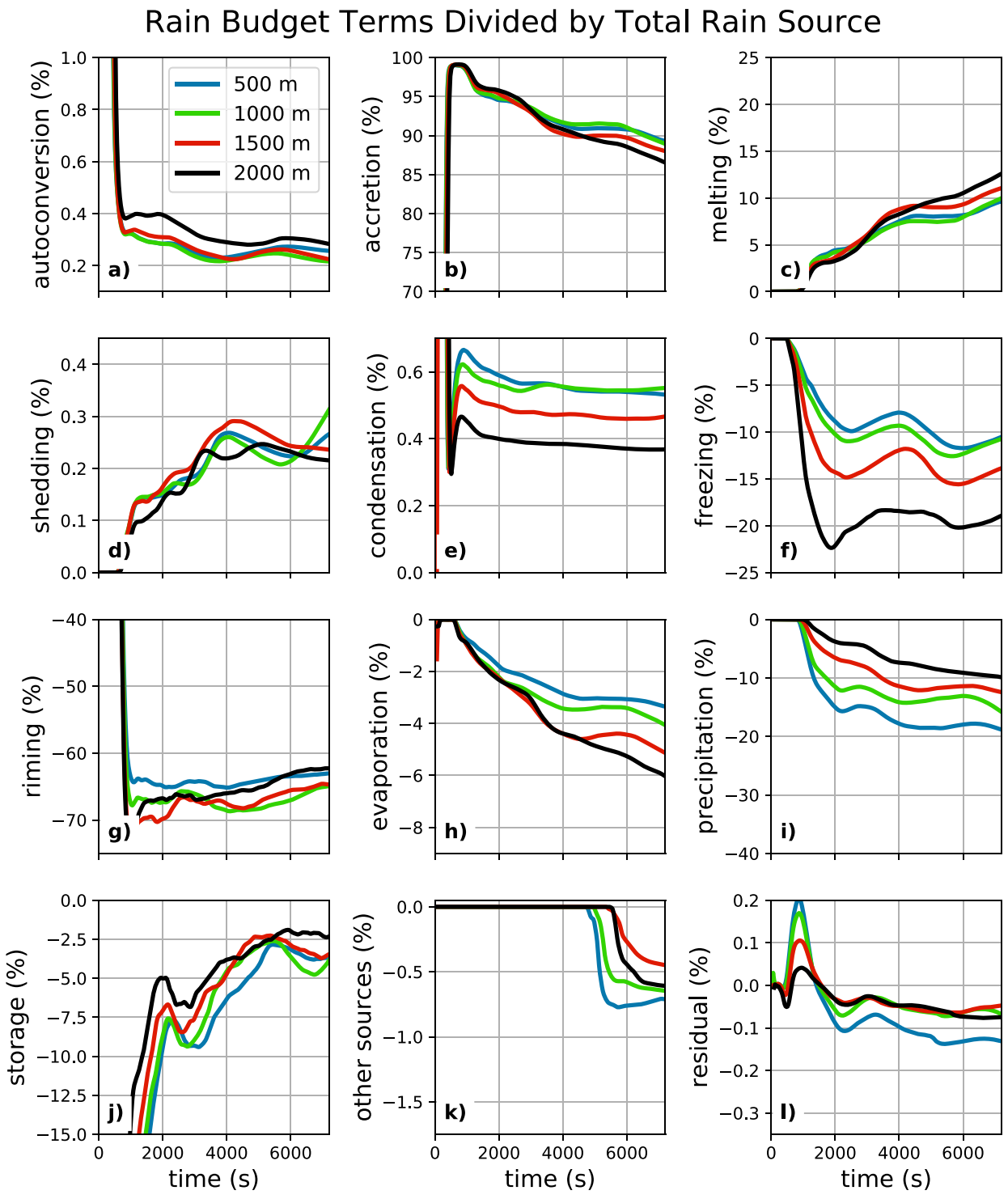

FIG. 8. Time series of rain budget terms for the control member of each ensemble. Budget terms are plotted as a percentage of the sum of all rain source terms, with source terms having positive percentages and sink terms having negative percentages.

melting on these rain budgets highlights the indirect impact that ice microphysics can have on cold pool strength by heavily influencing the amount of rain available for evaporation. In summary, it appears that an increase in environmental precipitable water and a decrease in the fraction of rain mass lost to freezing with lower LCLs are at least two reasons why low-LCL simulations tend to produce more rainfall than their high-LCL counterparts.

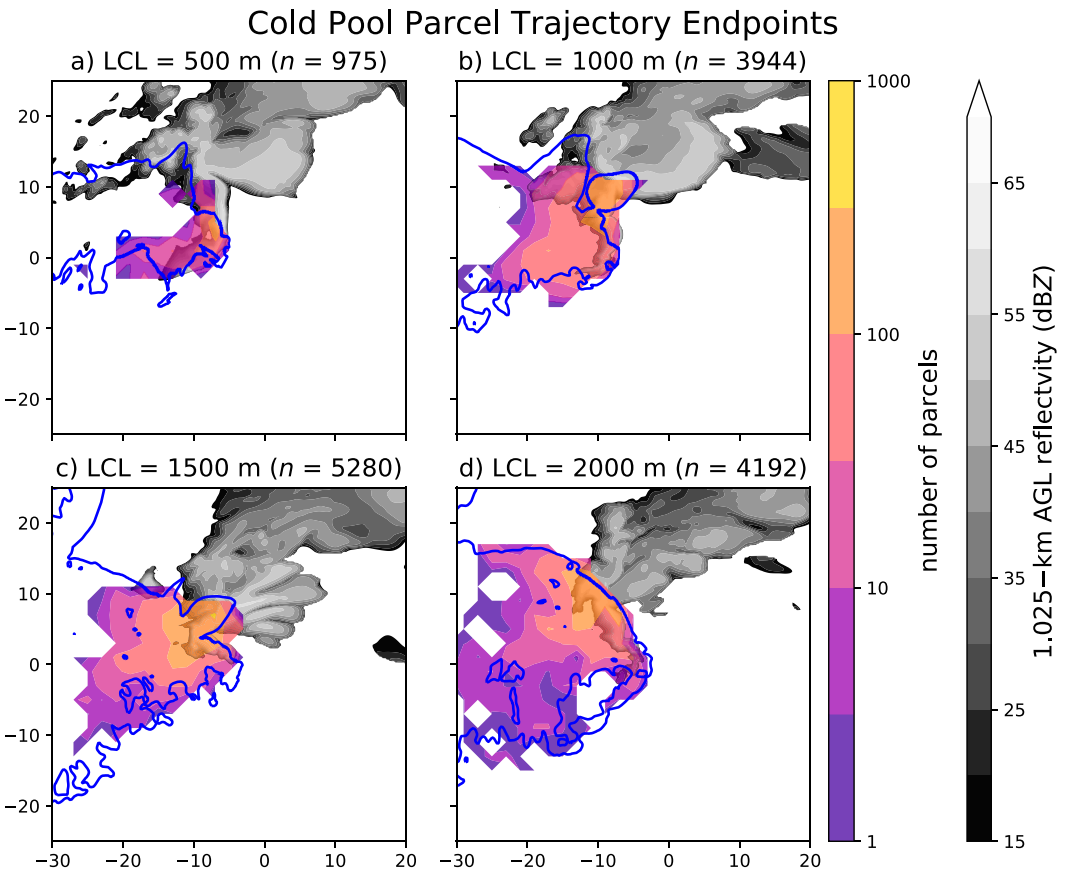

FIG. 9. Cold pool forward parcel trajectory endpoints for each control simulation. Parcel endpoints are binned into 2×2 km^2 bins, and the total number of parcels is listed in the subplot titles. The gray shading and blue contours depict reflectivity at 1.025 km AGL and the −1-K θ' contour at the LML, respectively, at 6300 s. Axis labels are in kilometers.

Although these Eulerian analyses are illuminating, we still cannot say why cold pool strength and sensitivity to the microphysics increase with higher LCLs. This is partially related to shortcomings of the Eulerian perspective, which make it difficult to determine how much processes occurring aloft contribute to the near-surface cold pool. For example, does cooling from melting at 3 km AGL directly contribute to near-surface cold pool strength? Or is it completely offset by compressional warming, as suggested by Mallinson and Lasher-Trapp (2019)? To answer such a question, information about the airflow within a supercell is required, which makes parcel trajectories a logical tool. Another shortcoming of the analyses presented in this section is that the role of other terms in the B equation, such as hydrometeor loading, is not considered. Buoyancy is the relevant measure to examine when determining cold pool strength, and microphysical cooling is just one process that contributes to negative B. Thus, we will use B budgets along parcel trajectories in an attempt to definitively answer our research questions.

4. Lagrangian analysis

Our Lagrangian analysis will start with the control members in order to examine some general characteristics of the B budgets. We will then examine aggregate statistics from all LCL = 500 m and LCL = 2000 m ensemble members to explain why the sensitivity of the cold pools to the microphysics increases with higher LCLs.

a. *Control simulations*

Parcel endpoints for the control simulations are shown in Fig. 9. The parcels generally terminate along the eastern edge of the cold pool within the rear flank of the storm, which is the portion of the cold pool that is most relevant for tornadogenesis and low-level updraft maintenance. The number of parcels identified ranges from 975 to 5280 and generally increases as cold pool strength increases (cf. Fig. 4a). The number of parcels, along with the endpoints of these parcels, gives us confidence that we are robustly capturing processes contributing to cold pool strength at the leading edge of the rear-flank cold pool.

Cold pool parcel B budgets for these control simulations can be used to determine the drivers of cold pool strength. Histograms of B budget terms indicate that changes in θ along parcel trajectories are the dominant contributor to final parcel B, with changes in θ_0 and q_{tot} playing a secondary role and changes in q_v and q_{v0} being almost negligible (Fig. 10).

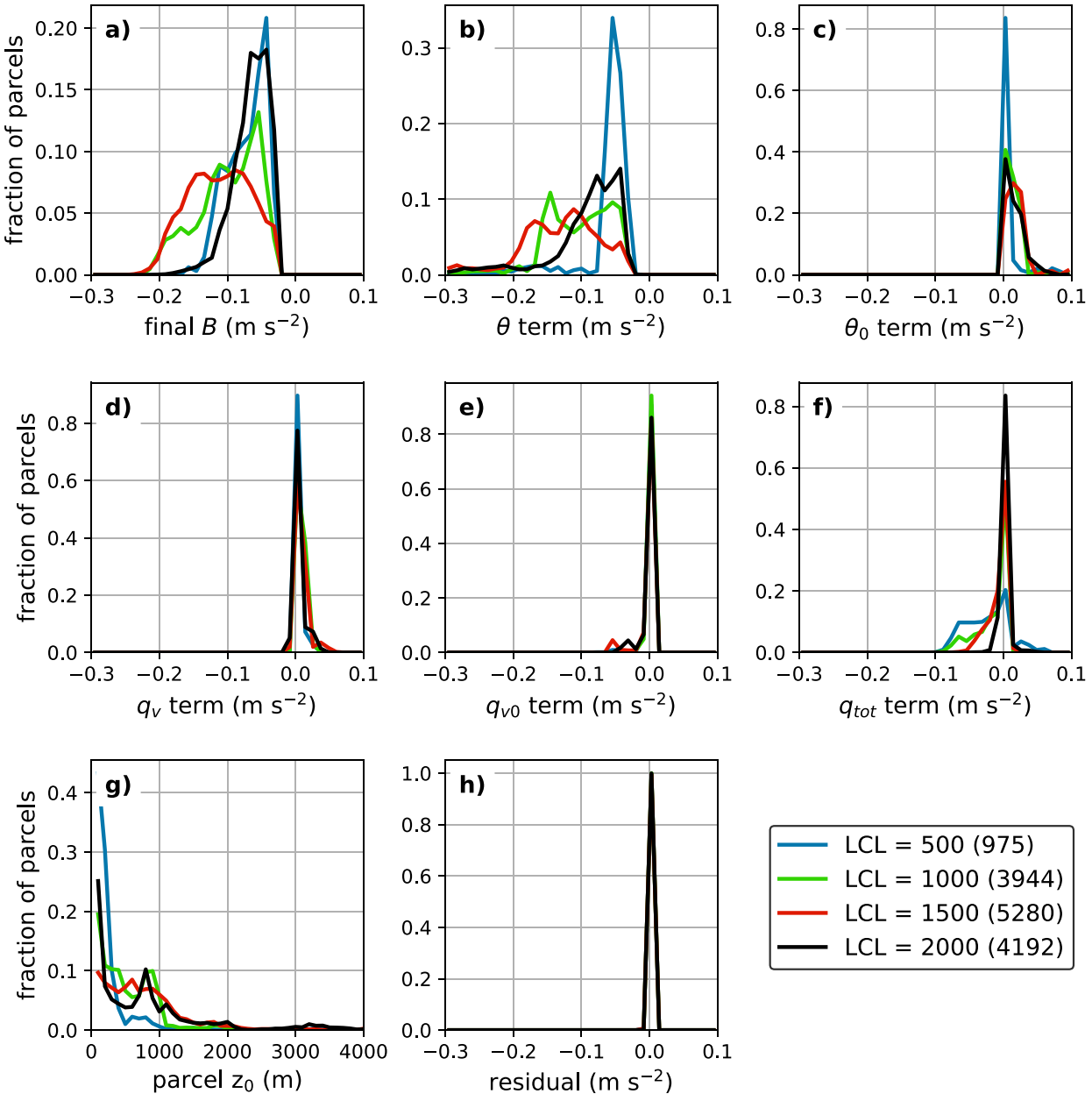

FIG. 10. Histograms of time-integrated buoyancy budget terms for parcels in the control simulations. Plotted quantities include (a) buoyancy interpolated to the final parcel location, (b)–(f) time-integrated buoyancy budget terms, valid at the final parcel location, (g) initial parcel height, and (h) the residual between the sum of all the time-integrated buoyancy budget terms and the interpolated buoyancy. The number of parcels in each simulation is given in the legend. Bin counts are divided by the total number of parcels for easier comparison.

Residuals for the B budgets are two orders of magnitude less than the final B values, indicating that our budgets are very accurate. Turning to microphysical processes that negatively impact θ, we find that rain evaporation is the dominant contributor (Fig. 11). This is unsurprising given that most of the parcels originate below 1000 m AGL (Fig. 10g), which is well below the maximum in melting and sublimation (Figs. 5e,g). Thus, even though melting and sublimation may cause cooling aloft and contribute to downdrafts, as shown by Mallinson and Lasher-Trapp (2019), these microphysical processes do not appear to directly contribute to the near-surface cold pool. Instead, rain evaporation appears to be the dominant driver of cold pool strength in supercells.

b. LCL = 500 m and LCL = 2000 m ensembles

Examining the mean contributions from each term in the B budget for all the parcels in the LCL = 500 m and LCL = 2000 m ensembles provides insight into two

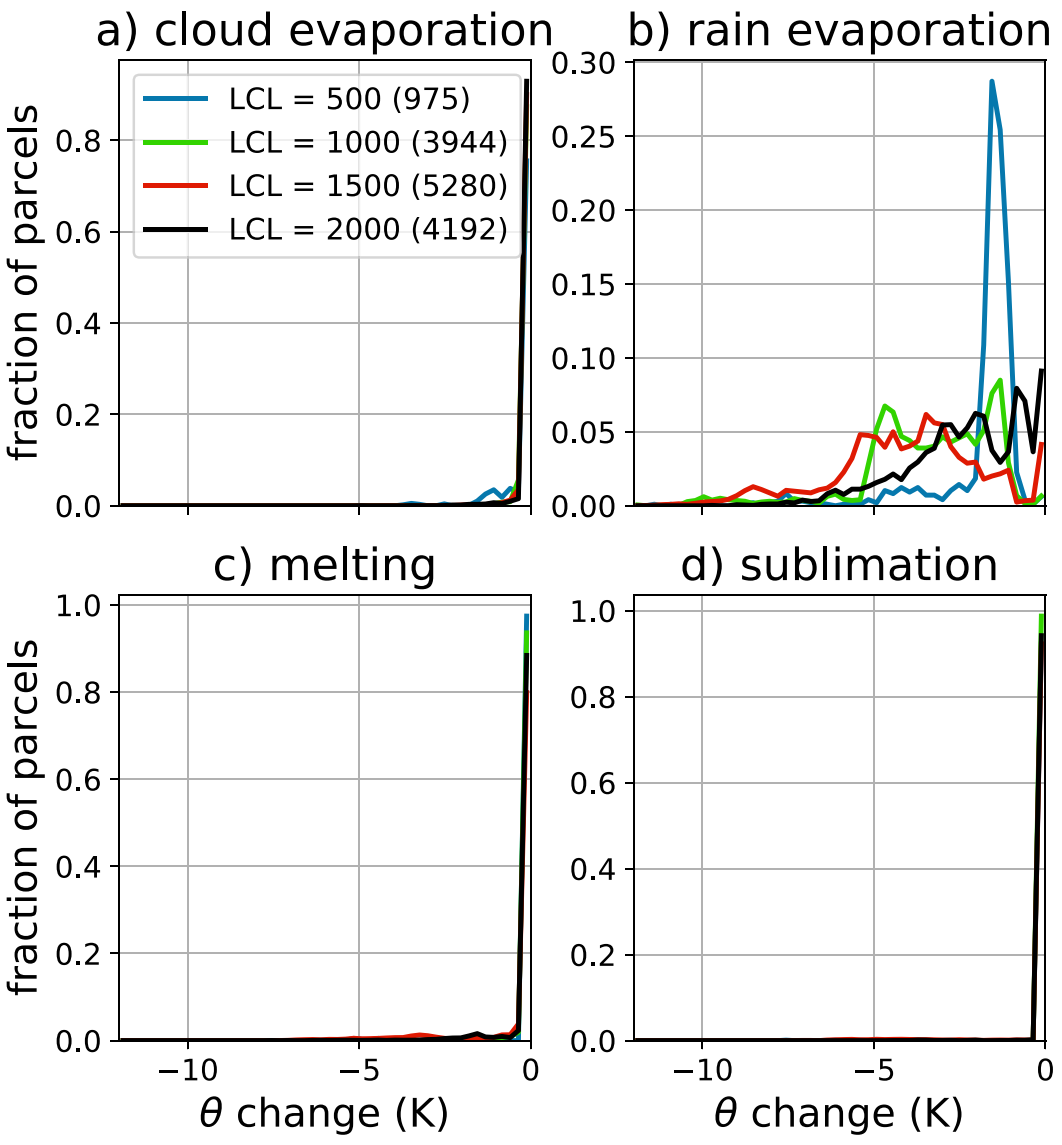

FIG. 11. As in Fig. 10, but for the microphysical cooling terms in the potential temperature budget.

observations made in section 3: 1) the sensitivity to the microphysics increases with higher LCLs and 2) the LCL = 2000 m ensemble has a stronger median cold pool strength compared to the LCL = 500 m ensemble despite both having similar low-level Q_{evar} profiles (Fig. 5c). Plots of the mean final B for all parcels in each simulation show a larger spread in the LCL = 2000 m ensemble compared to the LCL = 500 m ensemble (Fig. 12a), which agrees with the increase in ensemble spread of cold pool strength with higher LCLs shown in Fig. 4b. Examining the B budget terms shows that the spread in the means from each simulation is actually *larger* for the LCL = 500 m ensemble compared to the LCL = 2000 m ensemble (Figs. 12b–f). So how is it that the final B values have a larger spread in the LCL = 2000 m ensemble? The answer lies in the combination of the B budget terms, particularly the θ and θ_0 terms. When considering the sum of the θ and θ_0 terms, the spread is smaller in the LCL = 500 m ensemble (Fig. 12g), which agrees with the plot of the final B values in Fig. 12a. Thus, for these supercell simulations, both the θ and θ_0 terms must be considered in order to explain why the ensemble spread (and, therefore, the sensitivity to the microphysics) increases with higher LCLs.

This result that the sum of the θ and θ_0 terms need to be considered together to explain the increase in sensitivity to the microphysics with higher LCLs begs a closer examination of the behavior of these two terms. We will start with the θ_0 term. By assuming that $\theta \approx \theta_0$, we can rewrite the θ_0 term in a simplified form:

$$-g\int_{t_i}^{t_f}\frac{\theta}{\theta_0^2}\frac{d\theta_0}{dt}dt \approx -g\int_{t_i}^{t_0}\frac{1}{\theta_0}d\theta_0 = g\ln\frac{\theta_{0,i}}{\theta_{0,f}}, \tag{6}$$

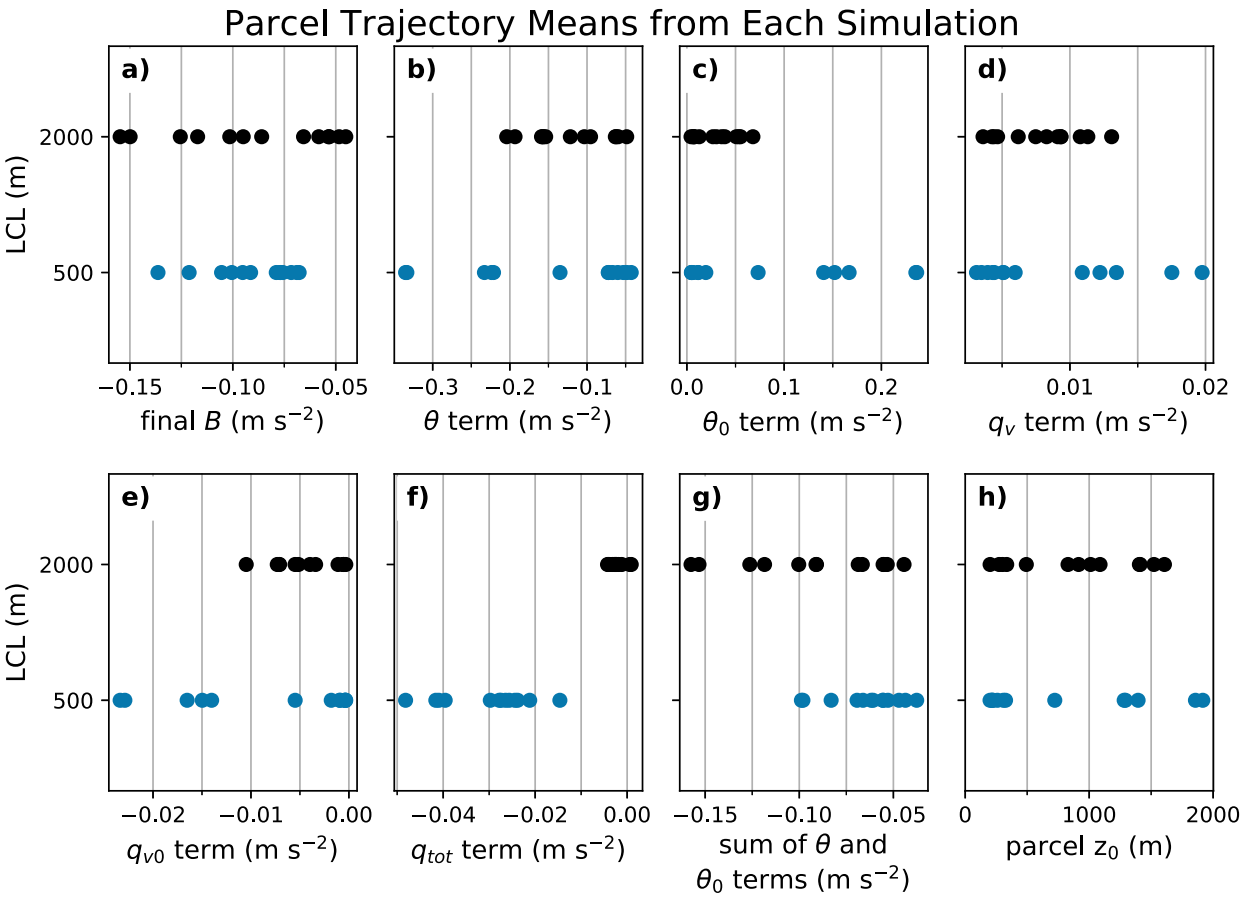

FIG. 12. Parcel buoyancy budget means from each of the LCL = 500 m and LCL = 2000 m ensemble members. Each dot represents the mean value from all parcels within that simulation. Plotted quantities include (a) buoyancy interpolated to the final parcel location, (b)–(f) time-integrated buoyancy budget terms, valid at the final parcel location, (g) sum of the time-integrated θ and θ_0 terms, valid at the final parcel location, and (h) the initial parcel height.

where $\theta_{0,i}$ and $\theta_{0,f}$ are θ_0 at the initial and final parcel positions, respectively. Our θ_0 profiles feature a nearly constant θ_0 profile below the LCL with a more pronounced increase in θ_0 with height above the LCL, which means that the LCL = 500 m base state will have a more rapid increase in θ_0 with height between 500 and 2000 m AGL compared to the LCL = 2000 m base state. Thus, for any altitude above 500 m, $\theta_{0,i}$ will be larger for a parcel from an LCL = 500 m simulation compared to an LCL = 2000 m simulation, resulting in a larger θ_0 term (Fig. 13a). Therefore, although the θ_0 term increases in magnitude for parcels that originate farther aloft, this increase is more rapid for the low-LCL simulations.

This same idea can be conceptualized by moving a parcel dry adiabatically from some height greater than 500 m down to the surface. As shown in Fig. 14, a parcel that descends from 1 km AGL will have a larger, positive $\Delta\theta$ at the surface when using the LCL = 500 m base state compared to the LCL = 2000 m base state. This large, positive $\Delta\theta$ is the contribution from the θ_0 term. This means that cold pool parcels in the low-LCL environments will have a larger, positive contribution from the θ_0 term. Thus, more microphysical cooling is required for the parcels in the low-LCL simulations to have similar negative θ' values in the cold pool as the parcels in the high-LCL simulations. This explains how the LCL = 2000 m simulations can have stronger cold pools than the LCL = 500 m simulations, despite both having similar low-level Q_{evar} profiles.

We now turn to the θ term. Figure 13b shows that the parcels with the most cooling originate from farther aloft. From this observation, we can conclude that the simulations with the largest, negative contributions from the θ term likely have more parcels contributing from farther aloft. Because these parcels originate farther aloft, they will also have larger, positive contributions from the θ_0 term. This gives us all the pieces we need to explain why high-LCL supercell simulations are more sensitive to the microphysics: Low-LCL simulations with large amounts of evaporational cooling contain more parcels that originate from farther aloft, which also have a large, positive contribution from the θ_0 term. Thus, these large, negative contributions from the θ term in the subset of the low-LCL simulations with the most evaporational cooling are countered by the large, positive contributions from the θ_0 term. This has a narrowing effect on the cold pool strength

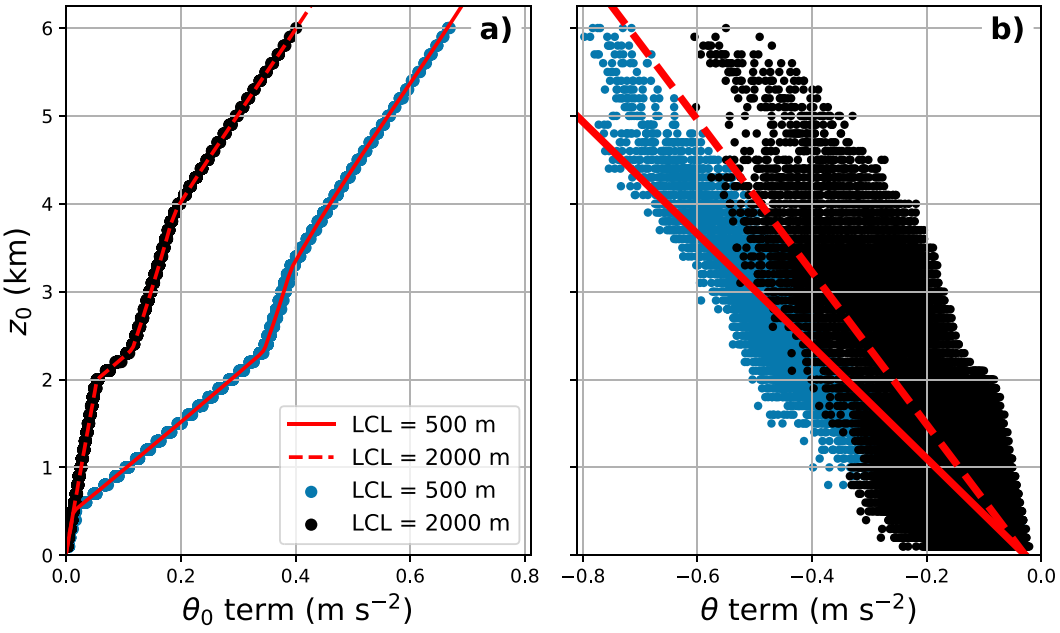

FIG. 13. Scatterplots of the time-integrated (a) θ_0 and (b) θ terms in the buoyancy budget as a function of parcel origin height for all parcels in the LCL = 500 m and LCL = 2000 m ensembles. Red solid and dashed lines in (a) show the approximation of the time-integrated θ_0 term from Eq. (6), while the red solid and dashed lines in (b) are least squares linear regression lines.

distribution. In the high-LCL ensemble, the countering effect of the θ_0 term is not as strong owing to the less rapid increase in θ_0 with height. Thus, the θ_0 term acts as a counterbalance to the large amounts of evaporational cooling in the coldest LCL = 500 m ensemble members, resulting in reduced ensemble spread and, therefore, reduced sensitivity to the microphysics.

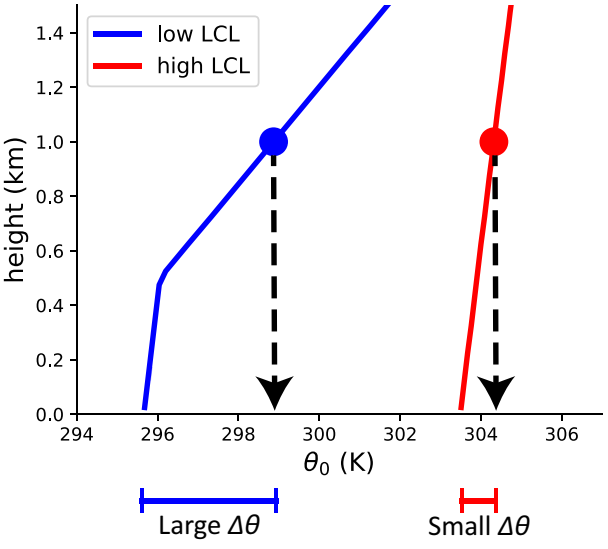

FIG. 14. Schematic illustrating how steeper potential temperature profiles are associated with larger, positive near-surface potential temperature perturbations $\Delta\theta$ when parcels descend dry adiabatically. Potential temperature profiles come from the LCL = 500 m (blue) and LCL = 2000 m (red) base states.

c. *Comparison to M22*

Given that the thermodynamic base states used in the current study and M22 are nearly identical, an open question is whether the physical mechanism described in the previous subsection also applies to the ordinary convection simulations of M22. To help answer this question, four ordinary convection simulations are performed using the same CM1 configuration outlined in section 2, except that the base-state environment does not contain any vertical wind shear. These simulations use the P3 configurations that produce the coldest (D_b = 100 μm, α_i = 1.5, and μ_r = 6) and warmest (D_b = 500 μm, α_i = 0.5, and μ_r = 0) cold pools with the LCL = 500 and 2000 m base states. Examining cold pool parcel *B* budgets for parcels released starting at 1800 s into the simulations suggests that the physical mechanism as to why the sensitivity of the cold pool to the microphysics increases with higher LCLs identified in the present study also appears in the simulations of ordinary convection (not shown). More specifically, parcels in the LCL = 500 m simulations tended to have larger, positive contributions from the θ_0 term in the *B* budget, and this counterbalanced the strong diabatic cooling in the LCL = 500 m simulation with the strongest cold pool, resulting in a smaller difference in cold pool strengths between the two LCL = 500 m simulations compared to the two LCL = 2000 m simulations. Thus, this mechanism does not appear to be restricted to the supercellular convective mode, at least when using the P3 scheme. We speculate that the physical mechanism identified here related to the θ_0 term and

the mechanism identified in M22 (that a drier PBL results in a greater evaporation potential that exaggerates microphysical uncertainties) both play a role in explaining why the sensitivity of cold pools to the microphysics increases with higher LCLs in the simulations of M22.

5. Conclusions

Previous research by M22 showed that the sensitivity of cold pools in ordinary convection to the microphysics scheme increases with the LCL. The current study explored whether those results were also applicable to supercells. While answering this question, we also explored the relation between the LCL and cold pool strength. To do this, four ensembles, each with a different LCL between 500 and 2000 m, were run using CM1. Each of the 13 ensemble members used a different variation of the P3 microphysics scheme, which allowed us to use ensemble spread as a proxy for the sensitivity to the microphysics. These P3 variations were guided by a sensitivity study that demonstrated that the raindrop breakup threshold, rain PSD shape parameter, and an ice fall speed multiplier were the most sensitive parameters out of a list of 12 parameters. It is recommended that future P3 development could focus on these aspects of P3 given the large impact they can have on cold pool strength.[4] The ensembles were analyzed using an Eulerian perspective, which relied on vertical profiles of microphysical processes, and a Lagrangian perspective, which focused on computing buoyancy budgets along parcel trajectories that terminated in the cold pool.

a. Key findings

Our analysis was guided by the three research questions from section 1. We offer the following answers to those questions:

1) Negative buoyancy in the cold pool was driven primarily by rain evaporational cooling, with hydrometeor loading and the θ_0 profile playing secondary roles. When θ_0 increased rapidly with height, the negative buoyancy in parcels that descend from aloft is largely eroded (owing to the colder near-surface θ_0 compared to θ_0 aloft, which decreases parcel $|\theta'|$), which reduces cold pool strength.
2) Cold pool strength generally increased with higher LCLs owing to a slight increase in rain evaporational cooling and a weaker increase in θ_0 with height. Rain evaporation did not vary strongly between the four ensembles owing to a decrease in rain mass and an increase in mean raindrop sizes with higher LCLs, which countered the tendency for greater evaporation with higher LCLs owing to lower humidities. The impact of the θ_0 profile on cold pool strength is particularly pronounced when considering the LCL = 500 m and LCL = 2000 m ensembles. Both had similar rain evaporation amounts, but the LCL = 500 m ensemble had a warmer cold pool owing to the steeper θ_0 vertical profile associated with that base state.
3) Similar to M22, the sensitivity of cold pools to the microphysics increased with LCL, though the physical mechanism differed from what was originally identified in M22. The steeper θ_0 profiles in the low-LCL supercells largely countered the large rain evaporational cooling in the coldest parcels that originated from aloft, reducing the cold pool strength in the simulations with the most rain evaporational cooling. This ultimately reduced the ensemble spread of cold pool strengths compared to the high-LCL ensembles, which did not experience as strong of a countering effect. This mechanism also appears to occur in ordinary convection, which suggests that the mechanism is not unique to supercells and that a combination of the mechanism identified here and the one identified in M22 can be responsible for the increase in cold pool sensitivity to the microphysics with higher LCLs.

Based on these results, it is clear that the claim that higher LCLs result in stronger cold pools owing to more rain evaporational cooling is nuanced. The LCL is related to the humidity in the PBL, which is one factor that controls evaporation (the "environmental control"), but the characteristics of the rain PSDs also matter (the "microphysical control"). When the microphysical control does not vary much with LCL, rain evaporation should increase with higher LCLs (e.g., M22). However, when the microphysical control does vary considerably with LCL, perhaps owing to more rainfall in low-LCL storms, then rain evaporation may not change much with LCL and may even *decrease* with higher LCLs (e.g., Lerach and Cotton 2012). This suggests that other environmental parameters that are related to precipitation production, such as precipitable water, may be useful in determining cold pool strength. Furthermore, rain evaporational cooling is not the only contributor to cold pool strength. In particular, the θ_0 vertical profile also plays a role. When θ_0 increases rapidly with height, the negative buoyancy in parcels that experience cooling farther aloft is largely eroded as the parcels descend. If θ_0 generally increases more rapidly with height in low-LCL environments, this could be another reason why low-LCL storms tend to have weaker cold pools.

b. Limitations and future work

Several updates to the P3 scheme have been made that were not available in CM1 when the simulations for this study were performed, and these updates will likely have some impact on our results. In particular, these updates include triple-moment rain (Paukert et al. 2019), triple-moment ice (Milbrandt et al. 2021; Cholette et al. 2023), and the option to predict the liquid fraction on ice particles (Cholette et al. 2019, 2023). All of these changes can impact the cold pool. Using triple-moment rain allows the shape parameter of the rain PSD to vary, which influences rain evaporation (Freeman et al. 2019) and, therefore, cold pool strength. Compared to a scheme using double-moment rain with a shape parameter of zero, using triple-moment rain would likely increase cold pool

[4] Some recent P3 developments do address these issues, such as the triple-moment rain parameterization (Paukert et al. 2019), which allows μ_r to be predicted, and the triple-moment ice parameterization (Milbrandt et al. 2021), which improves the representation of ice fall speeds. See section 5b.

strength (Dawson et al. 2010; Freeman et al. 2019). Using triple-moment ice tends to increase the amount of ice at low levels (Milbrandt et al. 2021; Cholette et al. 2023), which may increase the importance of melting and sublimation on cold pool strength. Using the predicted liquid fraction tends to increase cold pool strength (Cholette et al. 2023), which may further increase the importance of ice processes on cold pool strength. Taken altogether, using a newer version of P3 with these more physical updates may reduce the relative impact of rain evaporation on cold pool strength, which was the main focus of our study. How these updates to P3 impact our results is left to future investigators.

As alluded to above, perhaps the largest caveat in this study is that only a single base microphysics scheme was used. The fact that both this study and M22 found that the sensitivity of cold pools to the microphysics increases with higher LCLs while using different microphysics schemes gives us confidence that this result is likely insensitive to the microphysics scheme being used. However, it is possible that the physical reasoning as to *why* the sensitivity increases with LCL might differ with different microphysics schemes (as well as other conditions, such as base-state environmental parameters other than the LCL). As mentioned above, using a different base microphysics scheme may result in ice processes having a larger impact on cold pool strength, which may lead to yet another physical avenue as to why sensitivity to the microphysics increases with LCL (assuming that is still the case when this hypothetical microphysics scheme is used). Thus, it is best to frame this study as reporting yet another physical mechanism as to why high-LCL storms are more sensitive to the microphysics.

Future work can increase the robustness of these results by repeating these experiments with a different base microphysics scheme, using more realistic thermodynamic base states and using backward instead of forward trajectories to get coverage within other parts of the cold pool. Additionally, future studies can examine whether supercell hazards, such as tornadoes, are also more predictable in low-LCL environments. Preliminary research in this area suggests that tornadoes are more predictable in our low-LCL environment and the combination of a low LCL and a high LFC appears to impede tornado production (chapter 4; Murdzek 2022), but it is unknown exactly why this is the case. Finally, cold pool observations from field projects can be used to better understand what environmental parameters, in addition to the LCL, play a role in controlling cold pool strength. Such a study could help forecasters better predict cold pool strength in real-time.

Acknowledgments. Thanks go to Hugh Morrison, Matt Kumjian, Guido Cervone, Elissa Bartos, Luke LeBel, Aaron Wang, Dylan Steinkruger, and Chelsey Laurencin for useful discussions and comments on this work. Hugh Morrison is also acknowledged for his help with P3, and George Bryan is thanked for his tireless support of CM1. Several Python packages were used in this study, including NumPy, SciPy, Matplotlib, XArray, Pandas, and MetPy (May et al. 2021). Computing resources came from Penn State Roar and NCAR Cheyenne (Computational and Information Systems Laboratory 2019). This work was funded by the National Science Foundation (NSF) Graduate Research Fellowship Program under Grant DGE1255832. Any opinions, findings, and conclusions or recommendations expressed in this material are those of the authors and do not necessarily reflect the views of the NSF.

Data availability statement. CM1 configuration files, analysis code, and select model output can be found on the Penn State DataCommons (https://doi.org/10.26208/GTRQ-SN71). Python code used to generate the base-state soundings can also be found at https://github.com/ShawnMurd/MetAnalysis.

APPENDIX

P3 Sensitivity Tests

The sensitivity of supercell cold pool strength to 12 different parameters within P3 is examined, with the three most sensitive parameters being used for the perturbed-microphysics ensembles in this study. All 12 of these parameters are listed in Table A1, along with the default values used in the control simulation and the test values. The functions f, g, h, and F mentioned in Table A1 are as follows:

$$f(T, F_r) = \begin{cases} 0.1 \times f_{eii}, & T < 253.15\,\text{K} \\ \left(0.1 + 0.9\dfrac{T - 253.15}{15}\right) \times f_{eii}, & 253.15\,\text{K} \le T < 268.15\,\text{K} \\ f_{eii}, & T \ge 268.15\,\text{K} \end{cases}, \tag{A1}$$

where T is the temperature, F_r is the rime mass fraction, and

$$f_{eii} = \begin{cases} 1, & F_r < 0.6 \\ 1 - \dfrac{F_r - 0.6}{0.3}, & 0.6 \le F_r < 0.9 \\ 0, & F_r \ge 0.9 \end{cases} \tag{A2}$$

(Milbrandt and Morrison 2016). The functions $g(T)$ and $h(T, X_{WG})$ are the same as $f(T, F_r)$, but with $f_{eii} = 1$ everywhere in g and $f_{eii} = 0$ everywhere in h unless wet growth is occurring, in which case $f_{eii} = 1$. Function $F(\lambda_i)$ is given by Eq. (3) of Morrison and Milbrandt (2015). Interested readers are referred to chapter 2.2.4 of Murdzek (2022) for a detailed description of these parameters and a justification for the test values.

All sensitivity tests are performed using the same CM1 setup and base-state wind profile as discussed in section 2. The tests use the LCL = 1000 m thermodynamic profile without the nearly moist adiabatic layer above the LCL. Sensitivity is measured using $\Sigma B_{\text{sfc,CP}}$, with a maximum distance of either 30 or 4 km from the midlevel mesocyclone.

Mean differences in $\Sigma B_{\text{sfc,CP}}$ between pairs of simulations are plotted in Fig. A1. To arrive at the three most sensitive parameters, we selected the three that had the largest absolute mean difference in $\Sigma B_{\text{sfc,CP}}$ using a maximum distance

TABLE A1. Parameters used in the P3 sensitivity tests. See text for functions *f*, *g*, *h*, and *F*. CCN refers to cloud-condensation nuclei.

Parameter	Symbol	Default value	Test value(s)
Ice–cloud collection efficiency	e_{ci}	0.5	0.3, 1.0
Ice fall speed multiplier	α_i	1	0.5, 1.5
Ice–ice collection efficiency	e_{ii}	$f(T, F_r)$	$g(T)$, $h(T, X_{WG})$
Size of shed drops	D_{shd}	1 mm	0.5, 3.0 mm
Number of ice categories	N_{cat}	2	1
Number of CCN	N_{ccn}	3×10^8 kg^{-1}	1×10^8, 1.5×10^9 kg^{-1}
Evaporation coefficient	γ_{evp}	1	0, 0.5
Ice PSD shape parameter	μ_i	$F(\lambda_i)$	0, 6
Maximum allowed ice particle size	$D_{m,i}$	2 mm	40 mm
Rain PSD shape parameter	μ_r	0	3, 6
Maximum allowed raindrop size	$D_{m,r}$	4 mm	0.8 mm
Raindrop breakup threshold	D_b	280 μm	100, 500 μm

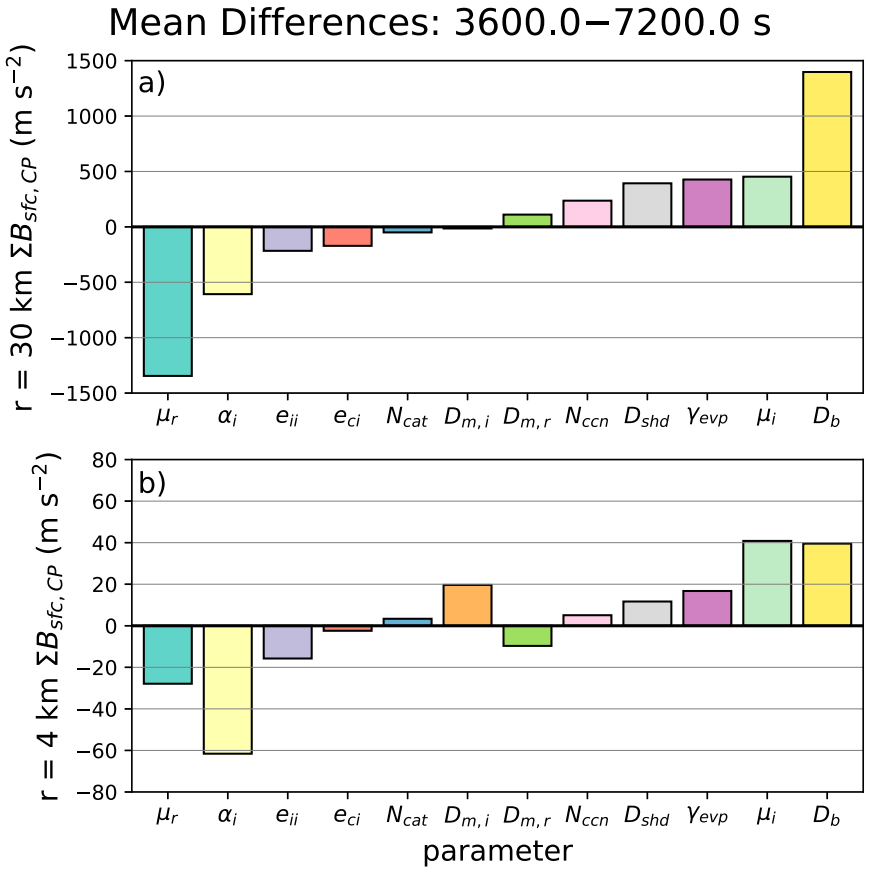

FIG. A1. Cold pool sensitivity to P3 parameters. (a) Differences in the total cold-pool buoyancy at the LML and within 30 km of the mesocyclone averaged over the second hour of the simulations. (b) As in (a), but only using grid points within 4 km of the mesocyclone. Differences come from the simulation with the highest value in Table A1 minus the simulation with the lowest value. Thus, positive (negative) mean differences indicate that cold pool strength decreases (increases) as that particular parameter increases. Definitions of the P3 parameters along the *x* axis are given in Table A1. For μ_i, the mean difference is the $\mu_i = 6$ simulation minus the $\mu_i = 0$ simulation. For e_{ii}, the mean difference is the $e_{ii} = g(T)$ simulation minus the $e_{ii} = h(T, X_{WG})$ simulation.

of 30 km from the midlevel mesocyclone. As seen in Fig. A1a, these parameters are D_b, μ_r, and α_i.

A brief discussion as to how changing D_b, μ_r, and α_i impacts cold pool strength is provided here, with a more in-depth discussion about these relationships, and how the other P3 parameters impact cold pool strength, found in chapter 2.2.4 of Murdzek (2022). Similar to Morrison and Milbrandt (2011) and Morrison et al. (2012), less aggressive raindrop breakup (i.e., larger D_b) results in fewer, larger raindrops that do not evaporate as readily as smaller raindrops. Less evaporation results in less cooling and a weaker cold pool. Assuming the total rain mass and rain number are constant, larger values of μ_r result in larger number-weighted mean raindrop diameters, which increases rain evaporation and, therefore, evaporational cooling (e.g., Freeman et al. 2019). Faster falling ice (i.e., larger α_i) results in a larger flux of ice into the melting layer, which contributes to more rain mass. This greater rain mass results in more evaporational cooling and colder cold pools (e.g., Morrison and Milbrandt 2011).

REFERENCES

Betten, D. P., M. I. Biggerstaff, and L. J. Wicker, 2017: A trajectory mapping technique for the visualization and analysis of three-dimensional flow in supercell storms. *J. Atmos. Oceanic Technol.*, **34**, 33–49, https://doi.org/10.1175/JTECH-D-16-0043.1.

Brown, M., and C. J. Nowotarski, 2019: The influence of lifting condensation level on low-level outflow and rotation in simulated supercell thunderstorms. *J. Atmos. Sci.*, **76**, 1349–1372, https://doi.org/10.1175/JAS-D-18-0216.1.

Bryan, G. H., 2021: The governing equations for CM1. NCAR Doc., 30 pp., https://www2.mmm.ucar.edu/people/bryan/cm1/cm1_equations.pdf.

——, and J. M. Fritsch, 2002: A benchmark simulation for moist nonhydrostatic numerical models. *Mon. Wea. Rev.*, **130**, 2917–2928, https://doi.org/10.1175/1520-0493(2002)130<2917:ABSFMN>2.0.CO;2.

Cholette, M., H. Morrison, J. A. Milbrandt, and J. M. Thériault, 2019: Parameterization of the bulk liquid fraction on mixed-phase particles in the Predicted Particle Properties (P3) scheme: Description and idealized simulations. *J. Atmos. Sci.*, **76**, 561–582, https://doi.org/10.1175/JAS-D-18-0278.1.

——, J. A. Milbrandt, H. Morrison, D. Paquin-Ricard, and D. Jacques, 2023: Combining triple-moment ice with prognostic liquid fraction in the P3 microphysics scheme: Impacts on a simulated squall line. *J. Adv. Model. Earth Syst.*, **15**, e2022MS003328, https://doi.org/10.1029/2022MS003328.

Coffer, B. E., M. D. Parker, J. M. L. Dahl, L. J. Wicker, and A. J. Clark, 2017: Volatility of tornadogenesis: An ensemble of simulated nontornadic and tornadic supercells in VORTEX2 environments. *Mon. Wea. Rev.*, **145**, 4605–4625, https://doi.org/10.1175/MWR-D-17-0152.1.

——, ——, R. L. Thompson, B. T. Smith, and R. E. Jewell, 2019: Using near-ground storm relative helicity in supercell tornado forecasting. *Wea. Forecasting*, **34**, 1417–1435, https://doi.org/10.1175/WAF-D-19-0115.1.

Cohen, C., and E. W. McCaul Jr., 2006: The sensitivity of simulated convective storms to variations in prescribed single-moment microphysics parameters that describe particle distributions, sizes, and numbers. *Mon. Wea. Rev.*, **134**, 2547–2565, https://doi.org/10.1175/MWR3195.1.

Computational and Information Systems Laboratory, 2019: Cheyenne: HPE/SGI ICE XA system. National Center for Atmospheric Research, accessed 30 May 2022, https://doi.org/10.5065/D6RX99HX.

Dawson, D. T., II, M. Xue, J. A. Milbrandt, and M. K. Yau, 2010: Comparison of evaporation and cold pool development between single-moment and multimoment bulk microphysics schemes in idealized simulations of tornadic thunderstorms. *Mon. Wea. Rev.*, **138**, 1152–1171, https://doi.org/10.1175/2009MWR2956.1.

——, ——, A. Shapiro, J. A. Milbrandt, and A. D. Schenkman, 2016: Sensitivity of real-data simulations of the 3 May 1999 Oklahoma City tornadic supercell and associated tornadoes to multimoment microphysics. Part II: Analysis of buoyancy and dynamic pressure forces in simulated tornado-like vortices. *J. Atmos. Sci.*, **73**, 1039–1061, https://doi.org/10.1175/JAS-D-15-0114.1.

Dowell, D. C., and Coauthors, 2022: The High-Resolution Rapid Refresh (HRRR): An hourly updating convection-allowing forecast model. Part I: Motivation and system description. *Wea. Forecasting*, **37**, 1371–1395, https://doi.org/10.1175/WAF-D-21-0151.1.

Freeman, S. W., A. L. Igel, and S. C. van den Heever, 2019: Relative sensitivities of simulated rainfall to fixed shape parameters and collection efficiencies. *Quart. J. Roy. Meteor. Soc.*, **145**, 2181–2201, https://doi.org/10.1002/qj.3550.

Gilmore, M. S., J. M. Straka, and E. N. Rasmussen, 2004a: Precipitation and evolution sensitivity in simulated deep convective storms: Comparisons between liquid-only and simple ice and liquid phase microphysics. *Mon. Wea. Rev.*, **132**, 1897–1916, https://doi.org/10.1175/1520-0493(2004)132<1897:PAESIS>2.0.CO;2.

——, ——, and ——, 2004b: Precipitation uncertainty due to variations in precipitation particle parameters within a simple microphysics scheme. *Mon. Wea. Rev.*, **132**, 2610–2627, https://doi.org/10.1175/MWR2810.1.

Grzych, M. L., B. D. Lee, and C. A. Finley, 2007: Thermodynamic analysis of supercell rear-flank downdrafts from project ANSWERS. *Mon. Wea. Rev.*, **135**, 240–246, https://doi.org/10.1175/MWR3288.1.

James, R. P., and P. M. Markowski, 2010: A numerical investigation of the effects of dry air aloft on deep convection. *Mon. Wea. Rev.*, **138**, 140–161, https://doi.org/10.1175/2009MWR3018.1.

Johnson, D. E., P. K. Wang, and J. M. Straka, 1993: Numerical simulations of the 2 August 1981 CCOPE supercell storm with and without ice microphysics. *J. Appl. Meteor.*, **32**, 745–759, https://doi.org/10.1175/1520-0450(1993)032<0745:NSOTAC>2.0.CO;2.

Johnson, M., Y. Jung, J. A. Milbrandt, H. Morrison, and M. Xue, 2019: Effects of the representation of rimed ice in bulk microphysics schemes on polarimetric signatures. *Mon. Wea. Rev.*, **147**, 3785–3810, https://doi.org/10.1175/MWR-D-18-0398.1.

Kacan, K. G., and Z. J. Lebo, 2019: Microphysical and dynamical effects of mixed-phase hydrometeors in convective storms using a bin microphysics model: Melting. *Mon. Wea. Rev.*, **147**, 4437–4460, https://doi.org/10.1175/MWR-D-18-0032.1.

Klemp, J. B., R. B. Wilhelmson, and P. S. Ray, 1981: Observed and numerically simulated structure of a mature supercell thunderstorm. *J. Atmos. Sci.*, **38**, 1558–1580, https://doi.org/10.1175/1520-0469(1981)038<1558:OANSSO>2.0.CO;2.

Lerach, D. G., and W. R. Cotton, 2012: Comparing aerosol and low-level moisture influences on supercell tornadogenesis: Three-dimensional idealized simulations. *J. Atmos. Sci.*, **69**, 969–987, https://doi.org/10.1175/JAS-D-11-043.1.

Mallinson, H. M., and S. G. Lasher-Trapp, 2019: An investigation of hydrometeor latent cooling upon convective cold pool formation, sustainment, and properties. *Mon. Wea. Rev.*, **147**, 3205–3222, https://doi.org/10.1175/MWR-D-18-0382.1.

Mansell, E. R., C. L. Ziegler, and E. C. Bruning, 2010: Simulated electrification of a small thunderstorm with two-moment bulk microphysics. *J. Atmos. Sci.*, **67**, 171–194, https://doi.org/10.1175/2009JAS2965.1.

——, D. T. Dawson II, and J. M. Straka, 2020: Bin-emulating hail melting in three-moment bulk microphysics. *J. Atmos. Sci.*, **77**, 3361–3385, https://doi.org/10.1175/JAS-D-19-0268.1.

Markowski, P. M., and Y. P. Richardson, 2014: The influence of environmental low-level shear and cold pools on tornadogenesis: Insights from idealized simulations. *J. Atmos. Sci.*, **71**, 243–275, https://doi.org/10.1175/JAS-D-13-0159.1.

——, J. M. Straka, and E. N. Rasmussen, 2002: Direct surface thermodynamic observations within the rear-flank downdrafts of nontornadic and tornadic supercells. *Mon. Wea. Rev.*, **130**, 1692–1721, https://doi.org/10.1175/1520-0493(2002)130<1692:DSTOWT>2.0.CO;2.

——, ——, and ——, 2003: Tornadogenesis resulting from the transport of circulation by a downdraft: Idealized numerical simulations. *J. Atmos. Sci.*, **60**, 795–823, https://doi.org/10.1175/1520-0469(2003)060<0795:TRFTTO>2.0.CO;2.

May, R. M., S. C. Arms, P. Marsh, E. Bruning, J. R. Leeman, K. Goebbert, J. E. Thielen, and Z. S. Bruick, 2021: MetPy: A Python package for meteorological data. Accessed 1 September 2020, https://doi.org/10.5065/D6WW7G29.

McCaul, E. W., Jr., and M. L. Weisman, 2001: The sensitivity of simulated supercell structure and intensity to variations in the shapes of environmental buoyancy and shear profiles. *Mon. Wea. Rev.*, **129**, 664–687, https://doi.org/10.1175/1520-0493(2001)129<0664:TSOSSS>2.0.CO;2.

——, and C. Cohen, 2002: The impact on simulated storm structure and intensity of variations in the mixed layer and moist layer depths. *Mon. Wea. Rev.*, **130**, 1722–1748, https://doi.org/10.1175/1520-0493(2002)130<1722:TIOSSS>2.0.CO;2.

McDonald, J. M., and C. C. Weiss, 2021: Cold pool characteristics of tornadic quasi-linear convective systems and other convective modes observed during VORTEX-SE. *Mon. Wea. Rev.*, **149**, 821–840, https://doi.org/10.1175/MWR-D-20-0226.1.

Milbrandt, J. A., and M. K. Yau, 2005: A multimoment bulk microphysics parameterization. Part II: A proposed three-moment closure and scheme description. *J. Atmos. Sci.*, **62**, 3065–3081, https://doi.org/10.1175/JAS3535.1.

——, and H. Morrison, 2016: Parameterization of cloud microphysics based on the prediction of bulk ice particle properties. Part III: Introduction of multiple free categories. *J. Atmos. Sci.*, **73**, 975–995, https://doi.org/10.1175/JAS-D-15-0204.1.

——, ——, D. T. Dawson II, and M. Paukert, 2021: A triple-moment representation of ice in the Predicted Particle Properties (P3) microphysics scheme. *J. Atmos. Sci.*, **78**, 439–458, https://doi.org/10.1175/JAS-D-20-0084.1.

Morrison, H., and J. Milbrandt, 2011: Comparison of two-moment bulk microphysics schemes in idealized supercell thunderstorm simulations. *Mon. Wea. Rev.*, **139**, 1103–1130, https://doi.org/10.1175/2010MWR3433.1.

——, and J. A. Milbrandt, 2015: Parameterization of cloud microphysics based on the prediction of bulk ice particle properties. Part I: Scheme description and idealized tests. *J. Atmos. Sci.*, **72**, 287–311, https://doi.org/10.1175/JAS-D-14-0065.1.

——, G. Thompson, and V. Tatarskii, 2009: Impact of cloud microphysics on the development of trailing stratiform precipitation in a simulated squall line: Comparison of one- and two-moment schemes. *Mon. Wea. Rev.*, **137**, 991–1007, https://doi.org/10.1175/2008MWR2556.1.

——, S. A. Tessendorf, K. Ikeda, and G. Thompson, 2012: Sensitivity of a simulated midlatitude squall line to parameterization of raindrop breakup. *Mon. Wea. Rev.*, **140**, 2437–2460, https://doi.org/10.1175/MWR-D-11-00283.1.

——, A. Morales, and C. Villanueva-Birriel, 2015: Concurrent sensitivities of an idealized deep convective storm to parameterization of microphysics, horizontal grid resolution, and environmental static stability. *Mon. Wea. Rev.*, **143**, 2082–2104, https://doi.org/10.1175/MWR-D-14-00271.1.

——, and Coauthors, 2020: Confronting the challenge of modeling cloud and precipitation microphysics. *J. Adv. Model. Earth Syst.*, **12**, e2019MS001689, https://doi.org/10.1029/2019MS001689.

Murdzek, S. S., 2022: Changes in the sensitivity of convective storms and tornadoes to the microphysics parameterization in environments with different lifting condensation levels. Ph.D. thesis, The Pennsylvania State University, 197 pp.

——, P. M. Markowski, Y. P. Richardson, and M. R. Kumjian, 2021: Should reversible convective inhibition be used when determining the inflow layer of a convective storm? *J. Atmos. Sci.*, **78**, 3047–3067, https://doi.org/10.1175/JAS-D-21-0069.1.

——, Y. P. Richardson, P. M. Markowski, and M. R. Kumjian, 2022: How the environmental lifting condensation level affects the sensitivity of simulated convective storm cold pools to the microphysics parameterization. *Mon. Wea. Rev.*, **150**, 2527–2552, https://doi.org/10.1175/MWR-D-21-0258.1.

Orf, L., R. Wilhelmson, B. Lee, C. Finley, and A. Houston, 2017: Evolution of a long-track violent tornado within a simulated supercell. *Bull. Amer. Meteor. Soc.*, **98**, 45–68, https://doi.org/10.1175/BAMS-D-15-00073.1.

Paukert, M., J. Fan, P. J. Rasch, H. Morrison, J. A. Milbrandt, J. Shpund, and A. Khain, 2019: Three-moment representation of rain in a bulk microphysics model. *J. Adv. Model. Earth Syst.*, **11**, 257–277, https://doi.org/10.1029/2018MS001512.

Peters, J. M., C. J. Nowotarski, and H. Morrison, 2019: The role of vertical wind shear in modulating maximum supercell updraft velocities. *J. Atmos. Sci.*, **76**, 3169–3189, https://doi.org/10.1175/JAS-D-19-0096.1.

Saleeby, S. M., B. Dolan, J. Bukowski, K. V. Valkenburg, S. C. van den Heever, and S. A. Rutledge, 2022: Assessing rain drop breakup parameterizations using disdrometer observations. *J. Atmos. Sci.*, **79**, 2949–2963, https://doi.org/10.1175/JAS-D-21-0335.1.

Shabbott, C. J., and P. M. Markowski, 2006: Surface in situ observations within the outflow of forward-flank downdrafts of supercell thunderstorms. *Mon. Wea. Rev.*, **134**, 1422–1441, https://doi.org/10.1175/MWR3131.1.

Snook, N., and M. Xue, 2008: Effects of microphysical drop size distribution on tornadogenesis in supercell thunderstorms. *Geophys. Res. Lett.*, **35**, L24803, https://doi.org/10.1029/2008GL035866.

Stanford, M. W., H. Morrison, A. Varble, J. Berner, W. Wu, G. McFarquhar, and J. Milbrandt, 2019: Sensitivity of simulated deep convection to a stochastic ice microphysics framework. *J. Adv. Model. Earth Syst.*, **11**, 3362–3389, https://doi.org/10.1029/2019MS001730.

Torri, G., and Z. Kuang, 2016: A Lagrangian study of precipitation-driven downdrafts. *J. Atmos. Sci.*, **73**, 839–854, https://doi.org/10.1175/JAS-D-15-0222.1.

van den Heever, S. C., and W. R. Cotton, 2004: The impact of hail size on simulated supercell storms. *J. Atmos. Sci.*, **61**, 1596–1609, https://doi.org/10.1175/1520-0469(2004)061<1596:TIOHSO>2.0.CO;2.

Van Weverberg, K., 2013: Impact of environmental instability on convective precipitation uncertainty associated with the nature of the rimed ice species in a bulk microphysics scheme. *Mon. Wea. Rev.*, **141**, 2841–2849, https://doi.org/10.1175/MWR-D-13-00036.1.

Wilks, D. S., 2011: *Statistical Methods in the Atmospheric Sciences.* 3rd ed. Elsevier, 676 pp.